Paper 2: The fluid evolution of the Froland area in the Bamble sector from peak P-T through cooling and uplift: implications for retrograde mineral paragenesis and PT evolution of the Bamble Sector

Bjørn Eske Sørensen
Department of Geology and Mineral Resources Engineering, Norwegian University of Science and Technology (NTNU), N7491 Trondheim, Norway
(bjorn.sørensen@ntnu.no)

Rune Berg Larsen
Department of Geology and Mineral Resources Engineering, Norwegian University of Science and Technology (NTNU), N7491 Trondheim, Norway
(rune.larsen@ntnu.no)

Abstract

Microthermometry on fluid inclusions that can be related to specific mineral paragenesis constrain the fluid evolution of the Froland area in the Bamble sector to four specific fluid inclusion assemblages (FIA1-4).

FIA1 Pure CO_2 in garnet quartz symplectites that are interpreted as partial melts in amphibolites. FIA1 corresponds to the fluid present during peak metamorphic conditions.

FIA2 Retrograde fluids comprising low CO_2 brines with salinity near the NaCl-KCl-KCl eutectic and coexisting with CO_2-rich low salinity H_2O-CO_2 mixtures.
After FIA2 fluids, CO_2 and other carbonic species are absent.

FIA3 Brines with 25 wt% NaCl and 6wt% $CaCl_2$.. FIA3 are hosted by quartz in quartz biotite gneisses. FIA3 relates to scapolitisation and replacement of rutile by titanite and the formation of high purity quartz.

FIA4 Primary inclusions in calcite and epidote cores. Salinities were determined as $CaCl_2$ equivalents by microthermometry and vary between 36 wt% in early FIA4 inclusions and 31 wt% in late FIA4 inclusions. Compositional variation in epidote with Xcz =70-75 in cores and Xcz=65 in rims imply that Fe^{3+} increased over time. This agrees with lowering of the fist melting temperatures in late FIA4 inclusions suggesting additional cations in solution.

All together the fluid evolution documents a high salinity averaging 30 wt% throughout cooling and uplift of the Froland area and that the saline fluids partially control the retrograde assemblages. Accordingly, the previously published PT-path of Froland is revaluated with PERPLEX modelling. In addition the well defined isochore

of FIA3 and Ti in quartz thermometry are used to support the new PT-path. Our results confirm the main features of the Nijland et al. (1993) cooling and uplift path. The following stages in the PT-X_{fluid} path could be constrained:

1*:* Simultaneous reactions di + phl + qz = san+tr and di+H_2O+CO_2 = tr+cc+qz in calcsilicates fixes PT at a pseudounivariant point. The presence of rutile together with sanidine and tremolite suggest reduced XH_2O in the fluid caused by the presence of salts and CO_2 in the fluid near the thermal maximum of the tremolite + cc + quartz assemblage. Accordingly, the PT-conditions were approximately 626°C and 7 kb. The total fluid composition for this stage is estimated to be XCO_2 = (n_{CO2}/(n_{CO2}+n_{H2O}) = 0.32, XH_2O = 0.68, wt%NaCl = wt_{NaCl}/(wt_{H2O}+wt_{NaCl})=0.30. Because sanidine + tremolite is not replaced by phlogopite + calcite + quartz during cooling and uplift we infer that XCO_2 decreased rapidly with falling temperatures.
2: MII (kyanite-chlorite-muscovite veins) and MIII (margarite + corundum) of Nijland et al. (1993) are overlapping in the PT stability fields. Both are alteration products of an assemblage originally comprising corundum + plagioclase. MII muscovite was stabilised by potassium rich fluids. Decreased potassium content/increased calcium content of the fluid stabilised margarite in favour of muscovite and formed the margarite + corundum assemblage. The stability of margarite + corundum in P-T space is considerably larger than reported by Nijland et al. (1993), who used the anorthite + $H_2O \leftrightarrow$ Mrg + Zo + SiO_2 equilibria to define the lower temperature boundary. However, the stability of zoisite is primarily a function of bulk/fluid composition hence zoisite may be stabilised along with margarite in most of the margarite + corundum PT stability field, only by modifying bulk composition. P-T condition of MII represents a relatively narrow temperature field from 450 to 550°C. Pressure is constrained by the stability of kyanite which defines the lower pressure limit to 4.5 kb.
3: The uplift path is constrained by the isochore of FIA3. The well preserved fluid inclusions suggest an uplift path that was sub parallel with the isochore. Uplift likely occurred at 300 to 400°C. Accordingly, the Froland lithologies experienced a P-drop from 5-7 kb to 2-3 kb at temperatures 100°C lower than the interpretation provided by Nijland et al.(1993).
4: The last stage is defined by coexisting prehnite/pumpellyite and fluid inclusion studies of Touret and Olsen(1985) imply 2-3 kb and 175-280°C.

Our results underline the importance of fluids in interpreting metamorphic mineral assemblages given that the position of the equilibria in P-T space varies considerably with changing fluid composition.
The shift between MII and MIII assemblages marks an important event in the metasomatic evolution of the Bamble sector when alteration shifted from sodic-potassic to sodic-calcic. The same change is recorded by the shift in fluid composition between FIA2 to FIA3.

1 Introduction

The retrograde fluid evolution of the Bamble sector is not well constrained although some studies report on brine fluids associated with alteration processes (e.g. Nijland and Touret, 2001; Nijland et al., 1998; Touret, 1985).

The aim of the current study is to focus on the importance of the fluid composition in regional shear zone complexes, such as the Bamble sector, in partially controlling the mineral assemblages. We aim at reconstructing important stages of the fluid evolution of the Bamble sector from upper amphibolite facies conditions through exhumation to greenshist facies condition. None of the previous studies were able to constrain the timing, evolution and importance of the fluid phase during exhumation of the Bamble rocks. Particularly, this study demonstrates that the stabilities of the retrograde mineral assemblage are affected by the fluid composition.

The preferred approach is to study fluid inclusion fluids associated with characteristic alteration assemblages. Lack of proper index assemblages in the alteration rocks inhibits precise PT-estimates, however, partially; this inhibition is overcome by thermodynamic modelling of phase diagrams. Partially, the stability of many retrograde mineral assemblages depends on the fluid composition. As a result, many of the previously published PT-paths are uncertain because neither do they quantify the role of the fluid composition nor the salinity of the fluid.

We demonstrate that high salinity fluids with a high capacity to transport and buffer the cation makeup of the host rock lithologies dominated the uplift path.

Our studies document four characteristic stages comprising each their FIA (fluid inclusion assemblages), here presented in chronological order.

FIA1: Partial melting in garnet amphibolite, fluid inclusions from quartz in garnet quartz symplectites. Found at locality 1 (Figure 1).

FIA2: Primary fluid inclusions in en-echelon quartz veins in amphibolite. Found in locality 3 (Figure 1).

FIA3: Inclusions in quartz related to recrystallisation of quartz in a fluid channel pattern and to replacement of plagioclase by scapolite at locality 2 (Figure 1). The quartz formed during infiltration of FIA3 and experienced localised strain softening and the formation of SGR (subgrain rotation recrystallisation) microstructures in quartzites. The geometry of these SGR structures in quartzites suggest that they formed during thrust related deformation in an oblique slip pattern, controlled by the combination of pre-existing weakness directions and a N-S compressive stress field (paper 1, Sørensen and Larsen, 2007). Accordingly, the fluids belonging to FIA3 pose an important control upon the rheological properties of the Bamble rocks during exhumation.

FIA4: Primary inclusions in calcite and in epidote in a calcite-epidote-tremolite-apophyllite calcsilicate assemblage at locality 2 (Figure 1). They are associated with an assemblage that intersects all other observed alteration types. It is barely deformed hence is may have formed late during uplift or even later. The calcite-epidote-tremolite assemblage belongs to a series of complex calcsilicate assemblages formed during

retrogression of a phlogopite-diopside rock. The retrograde assemblages associated with these fluids are the result of hydration and chemical alteration during exhumation. Cation exchange between the fluids and the silisic gneisses and amphibolites, determines the stable mineral assemblage. The results from the fluid inclusion studies are used to re-evaluate the retrograde PT-path for the Froland area.

2 Geological setting

The Bamble sector comprises exceptionally well preserved high grade amphibolite-granulite facies rocks. Most authors agree that peak PT-conditions were c. 850 °C in the HT granulite facies zone at Arendal, and tapering towards lower T in a thermal dome pattern. Peak P was roughly 6-7 kbar.

Fluid inclusion studies document CO_2 dominated fluids in amphibolite lithologies, and CO_2 + brines in more siliceous gneisses (Touret, 1971). This COH fluid composition is matched by fluid modelling using the iron-titanium oxygen barometer (Harlov, 2000). The conditions during exhumation are far less constrained although the absence of retrograde aluminous silicate assemblages imply high alkali-chloride activities in the retrograde fluids (Touret, 1968). Knudsen (1996) summarise the available retrograde PT-paths of the Bamble sector and conclude that the PT-paths display systematic spatial variations characterised by a steep retrograde path in the southernmost part (Knudsen, 1996), followed by isobaric cooling in the southeast and a slight pressure increase in the north. However, it is also concluded that the P-T estimates are uncertain.

The publication of Nijland and co-workers (1993) is the only study to quantify the retrograde PT-path of the Froland area. Their results imply a 5 stage cooling path: MI (750°C, 7 kb), MII isobaric cooling (600-700°C, 7kb), MIII exhumation and rehydration (500-570°C 3-7 kb), MIV (400°C, 2-4 kb), MV (175-280°C, 2-3 kb). (Cosca et al., 1998) modelled the PT-t path with the Nijland data:

1. Near isobaric cooling at 7 kb and 750-600 °C, dP/dT = 2 bars/°C, DT/dt= 3-8°C/Ma.
2. Exhumation dP/dT = 30 bar/°C, dP(depth)/dt=0.5-1 mm/a, Dt/dt=2-4°C/My.3.
3: Bamble rocks remained at a depth of approximately 10 km while slowly cooling until ~200 Ma (e.g. Nijland et al., 1993).

Although the fluid evolution is poorly known it is stated that fluid related alteration follows a rhombohedral net work of shearzones and faults, associated with exhumation and possibly also extensional collapse of the Sveconorwegian mountain range. Brine-rich fluid inclusion are documented together with the alteration assemblages (e.g. Nijland and Touret, 2001; Nijland et al., 1998; Touret, 1985).

Intense metasomatic alteration is common along retrograde shearzones (Touret, 1968). Aqueous inclusions are interpreted as late, and there is a tendency towards density increase for progressively younger fluid inclusions (Touret and Olsen, 1985). However, aqueous brine inclusions have high densities but are interpreted as early

(Touret and Olsen, 1985). The exact timing and petrological significance of the retrograde aqueous/aqueous brine inclusions are not resolved (Touret and Olsen, 1985).

Calc-silicate rocks are common in the Bamble sector in both granulite (Bugge, 1943; Bugge, 1945; Bugge, 1940; Nijland and Maijer, 1993) and amphibolite facies (Barth and Dons, 1960).

Studies of amphibolites and quartzites preserves the retrogression as the result of episodic influx of brine fluids in discrete fractures during exhumation (paper 1 and 3, Sørensen and Larsen, 2007; Sørensen et al., 2007).

Furthermore, fluid related quartz recrystallisation textures correlate with thrust related quartz microstructures, testifying to the important role of hydrolytic weakening of quartz in the exhumation process. Similar observations were done in the Modum area (north Bamble sector), where the infiltrating fluids were mixtures of basinal brines and biogenetic carbonic fluids (Gleeson et al., 2003; Munz et al., 1994; Munz et al., 1995; Munz et al., 2002). Gleeson et al. (2003) also underlined the importance of hydrolytic weakening facilitated by retrograde fluids in the exhumation processes in the Modum area.

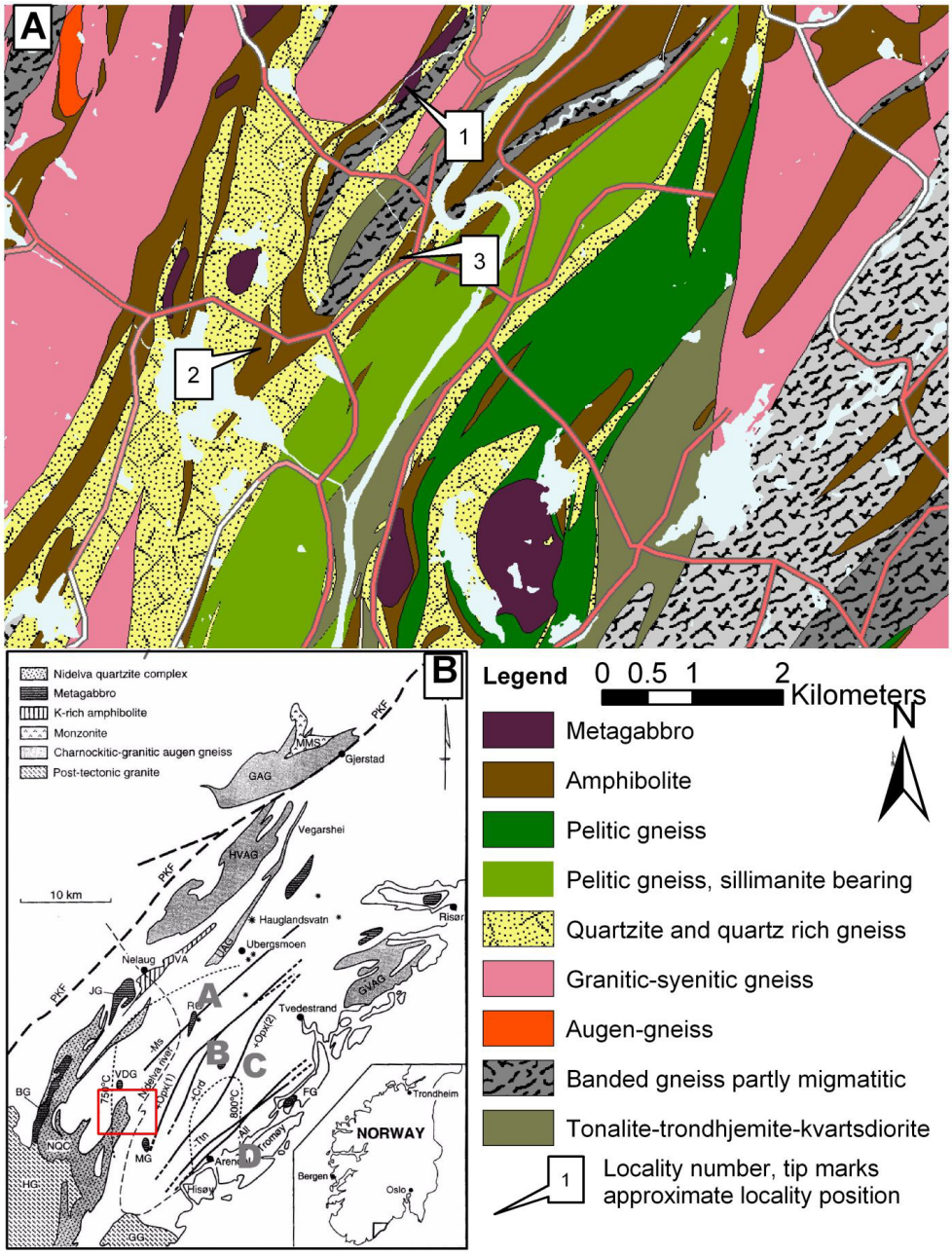

Figure 1: Geological maps. A) Detailed map of the investigated area. Modified from Geological Survey of Norway. N-50 berggrunns kart 16123 Nelaug and 16114 Arendal. Geographic data (roads, lakes and rivers) are added for easy orientation (source: www.geonorge.no). B) Overview map of the Bamble sector displaying the most important

rock units (see legend on map). Insert show the position of the Bamble Sector in South Norway. Red square denotes the position of the study area shown in A. From Nijland et al. (1998). Also shown in A are the metamorphic zones in the Bamble Sector.)

---

3 Field and petrographic observations

3.1 Calc-silicates.

The calc-silicate rocks used in this study comprise a metre thick layer sandwiched between quartz biotite plagioclase microcline gneiss and amphibolite at locality 2 (Figure 1). It is interpreted as a reactionskarn formed at the expense of the host rocks.

The high temperature assemblage comprises diopside + phlogopite+ titanite (Mp1 Table 1). This assemblage is only stable at high P and T, with the lower T stability limit dropping with increasing pressure (see also discussion). The calc-silicates experienced fluid aided retrograde alteration. Mp 1 is preserved in lensoid bodies. Alteration towards the amphibolite comprises biotite and amphibole (Mp2c) giving a gradual transition from the Fe-rich amphibolite to the Mg-rich calc-silicate rock (Figure 3). Alteration of the Mp1 assemblage against the silisic gneiss comprises microcline, actinolite and rutile/titanite (Mp2a) (Figure 3).

Mp1 is also intersected by two types of vein replacements named Mp2b: pyrrhotite + calcite veins and calcite veins mostly intersecting and replacing diopside (Figure 3). The pyrrhotite bearing veins mainly occurring toward the amphibolite, suggest that Fe was supplied by the amphibolite (Figure 3). Metasomatic zones are surrounding Mp1 and are comprised of tremolite, calcite, quartz and pyrrhotite. Considerable metasomatic differentiation is observed in relation to the Mp2 assemblage, giving zones comprising pure tremolite.

M2a-b assemblages are intersected by veins comprising new diopside, orthoclase, albite, pyrrhotite and titanite (Mp3). The diopside formed in Mp3 is Mg-rich but has a significantly higher Fe content than the Mp1 diopside (Table 2).

Phlogopite is unaffected by Mp2-3 but is replaced in a later assemblage by clinochlore and muscovite in an assemblage comprising tremolite pyrrhotite, graphite and minor molybdenite (Mp4). Pyrite is also present in the Mp4 samples, but comprises fingering veins intersecting the Mp4 assemblage.

Mp5 is the last of the calcsilicate assemblages comprising epidote, calcite, tremolite, pyrite and apophyllite. Mp5 also occurs in bands intersecting the foliation in the gneiss.

All the Fe-Mg phases except for epidote approach the Mg-endmembers (Table 2, Figure 2). The amphiboles comprises both edenite and tschermakite substitutions, with constant Mg/Fe ratio of 0.9 (Figure 2). Accordingly it is the Na-Al-Fe proportions that control their classification.

Table 1: Alteration stages in calc-silicate rocks.

Name	brief description	mineralogy	Occurrence/paragenises
Mp1	Diopside phlogopite veins	Diopside, Phlogopite, minor apatite	Meter thick lensoid bodies/layers at the boundary between quartz biotite-tourmaline-plagioclase gneiss and amphibolite. In some places it occurs together with carbonate bearing rocks
Mp2a	Microcline-tremolite massive metasomatic rock	Microcline, tremolite/actinolite, rutile/titanite and zircon. Calcite occurs with titanite and tremolite but not with rutile. Rutile occurs together with sanidine and tremolite but never with calcite.	Marginal alteration of Mp1 toward the quartz-biotite-plagioclase-tourmaline gneiss. Comprises coarse- and fine-grained parts. Rutile is partly replaced by titanite. Rutile is better preserved in more coarse-grained parts and occurs along with calcite, whereas titanite predominates in the fine-grained parts. The boundary toward Mp1 is smooth whereas the boundary toward the gneiss is gradual
Mp2b	Tremolite-calcite veining intersecting Mp1	Veins: Tremolite, calcite ± pyrrhotite. Metasomatic sides: quartz, titanite, tremolite.	Intersects Mp1 and alters it. Vein thickness varies between cm to mm size and is observed as greenish stripes intersecting the cream coloured Mp1 diopside matrix. Pyrrhotite bearing veins are recognized by rusty stains.
Mp2c	Phlogopite/ biotite-tremolite/magnesiohorblende	Tremolite/-magnesiohornblende, biotite, pyrrhotite and apatite	Not truly calc-silicate but reaction between the calcsilicate and the neighbouring amphibolite.
Mp3	Tremolite-dioside-albite-orthoclase veining	Veins: Tremolite, diopside, albite untwinnned occur intergrown with orthoclase. Calcite also present	Intersects apparently unaffected monomineralic tremolite, belonging to Mp2b. Secondary muscovite is common and clinozoisite commonly forms next to pyrrhotite grains. Tremolite grows into the vein, but is chemically similar to the tremolite surrounding the vein.
Mp4	Clinochlor, clinozoisite, graphite bearing assemblage.	Clinozoisite, clinochlore, tremolite, graphite, molybdenite, Pyrrhotite and chalcopyrite	Replacement of Mp1.Field observations testify that it is younger than Mp1, Mp2a, Mp2b and Mp2c.
Mp5	Tremolite-epidote-calcite around calcite-apophyllite vug fillings	Calcite, Epidote, Tremolite, pyrite and flour apophyllite	Marginal alteration of Mp1+Mp2b toward the quartz-biotite-plagioclase-tourmaline gneiss. Depend on addition of chemical components SiO_2 and Al_2O_3 from the gneiss. Similar assemblages seen in gneiss intersecting all other alterations on the field scale. The Fe needed for epidote formation supplied by replacement of pyrrhotite by pyrite.

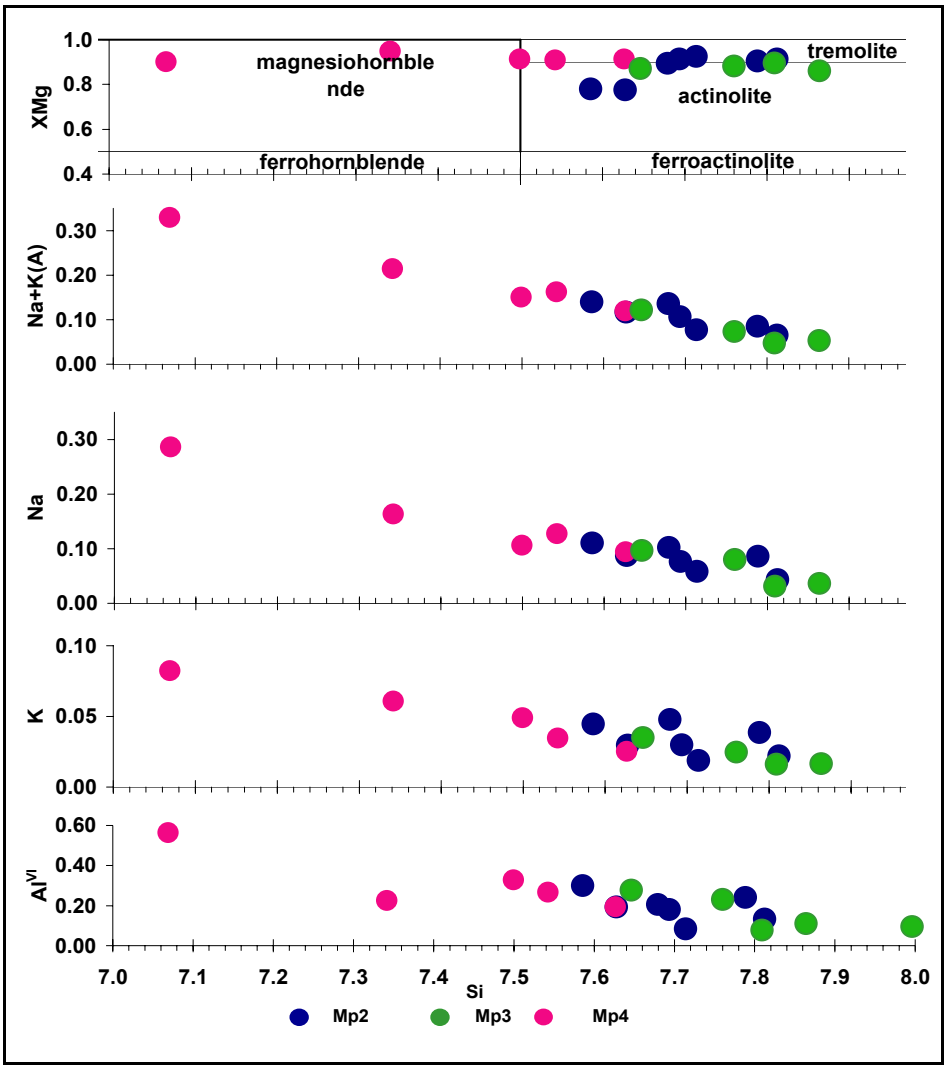

Figure 2 : amphibole chemistry in calc-silicate rocks. Note the increased edenite and tscermakite subitution in MP4 compared to Mp2 and Mp3

Table 2: Representative analyses of phases in the calc-silicate assemblages.

	Pyroxene				Phlogopite	Chlorite	Muscovite
	Mp3		Mp1		Mp1	Mp4	Mp4
	average	Std.dev	average	Std.dev			
				Oxide			
SiO_2	54.309	0.603	53.633	0.431	39.268	29.206	45.471
Al_2O_3	0.221	0.083	0.559	0.220	16.667	20.125	36.067
FeO	3.961	0.480	2.458	0.187	6.058	4.829	0.049
MnO	0.211	0.024	0.101	0.016	0.082	0.053	0.000
MgO	15.566	0.293	16.676	0.190	20.719	29.606	0.000
CaO	25.164	0.213	25.453	0.076	0.000	0.007	0.048
Na_2O	0.089	0.037	0.154	0.035	0.129	0.009	0.143
K_2O	0.026	0.020	0.019	0.018	10.128	0	9.983
TOTAL	99.547	0.806	99.054	0.525	93.051	83.835	91.761
H_2O*)	-	-	-	-	4.105	16	4.397
Calculated formulas							
					22 oxygen	28 oxygen	22 oxygen
Si	2.002	0.007	1.978	0.008	5.736	5.74	6.202
Al^{iv}	0.002	0.003	0.022	0.008	2.264	2.26	1.798
Al^{vi}	0.008	0.005	0.003	0.002	0.606	2.41	3.999
$Fe^{3+*)}$	0.006	0.010	0.047	0.011	no est.	0.08	no est.
Fe^{2+}	0.117	0.017	0.028	0.005	0.740	0.71	0.006
Mn	0.007	0.001	0.003	0.000	0.010	0.01	0.000
Mg	0.855	0.017	0.917	0.007	4.512	8.67	0.000
Ca	0.994	0.009	1.006	0.003	0.000	0.00	0.007
Na	0.006	0.003	0.011	0.002	0.037	0.01	0.038
K	0.001	0.001	0.001	0.001	1.887	0.00	1.737
OH*	-	-	-	-	4.000	16.00	4.000
TOTAL	3.997	0.007	4.016	0.004	19.791	35.90	17.787
XMg	0.874	0.018	0.967	0.005	0.859	0.92416222	-
Wo	50.072	0.196	49.978	0.105	-	-	Y total
En	43.103	0.780	45.564	0.391	-	-	4.005
Fs	6.504	0.768	3.912	0.277	-	-	X total
Ac	0.321	0.132	0.547	0.123	-	-	1.781
*) Fe3+ from Droop in pyroxene. Fe2+/Fe3+ and OH calculated assuming full site occupancy in Phlogopite							Al total 5.798

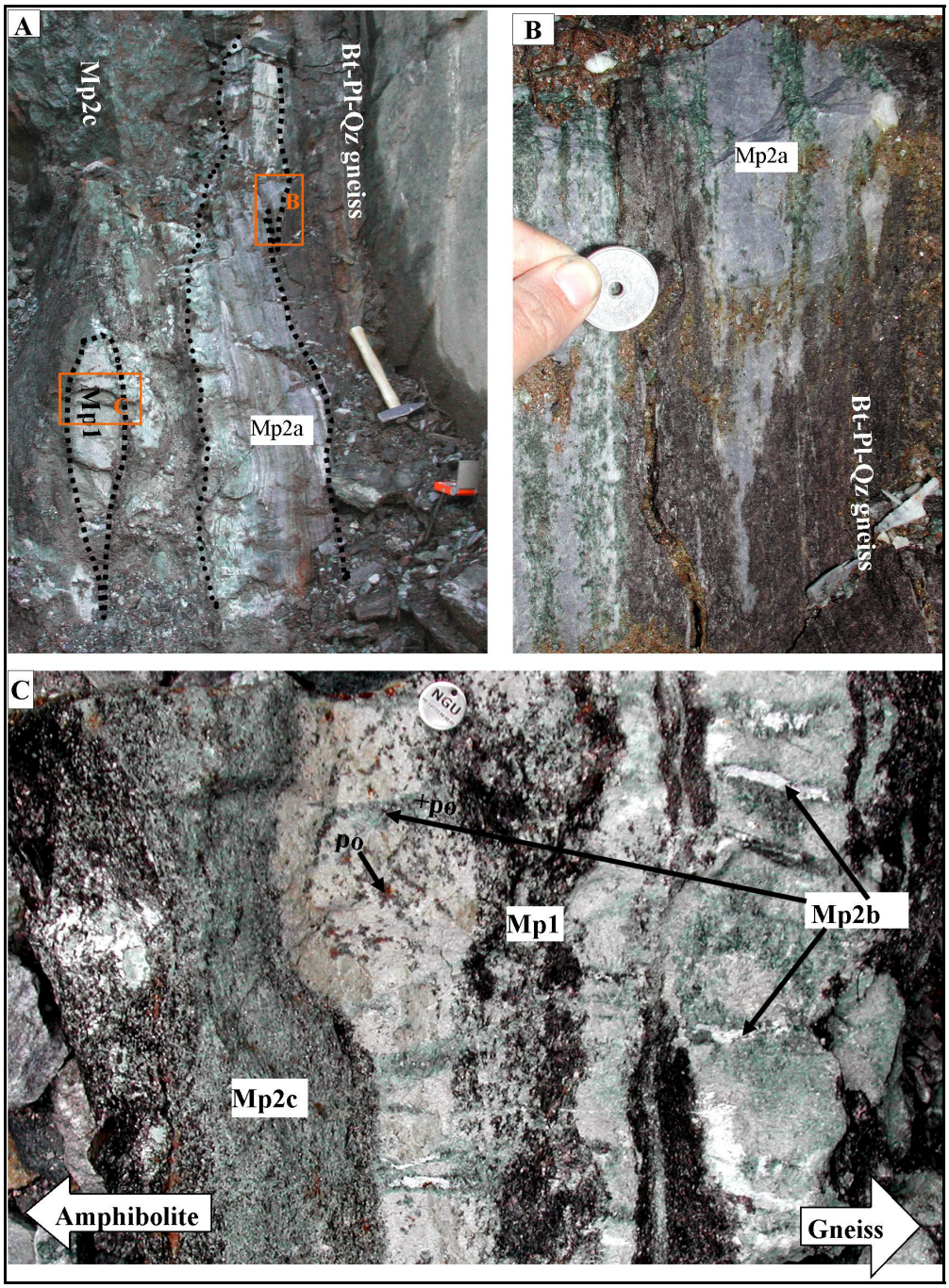

Figure 3: Field image displaying the relation between calc-silicate assemblages Mp1, Mp2a, Mp2b and Mp2c formed in calc-silicate body squeezed between amphibolite and

gneiss. A) Overview. B) Detail showing Mp2a and gneiss. C) Detail of calc-silicate body, intersected by Mp2b veins, note that pyrrhotite primarily occurs toward the amphibolite, suggesting that Fe was supplied by the amphibolite.

3.2 Amphibolites

The amphibolites experienced a complex metamorphic evolution as discussed in detail by Sørensen, Austrheim & Larsen (2007, paper 3). The first retrogressive event comprises potassium addition under the growth of biotite and rims on amphiboles (Alt1, Table 3) under the formation of decussate magnesiohornblende, biotite, plagioclase and ilmenite along en echelon quartz veins and plagioclase-calcite-pyrrhotite veins (Table 3). Biotite and plagioclase forming during Alt1 are locally replaced by k-feldspar (Alt2). Late scapolitisation (Alt3) involves replacement of plagioclase by scapolite in the titanite stability field without altering the amphiboles. The amphibolite alteration (Alt1) represent a wide range of amphibole compositions, following the pargasite substitution vector from ferro-tschermakite/(pargasite) (XMg = 0.3) to actinolite(XMg = 0.9)(paper 3, Sørensen et al., 2007) and occurred during falling temperatures. A more detailed description of the alteration of the amphibolites are given in Table 3 and in Sørensen et al. (2007, paper 3).

3.3 Quartzites, quartz rich gneisses and quartz veins

Sørensen and Larsen (paper 1, 2007) used SEM-CL and LA-ICP-MS to define the recrystallisation path of quartzites along the cooling and uplift path of the Bamble sector. Four main types of quartz are recognised:
Qz1: Bright islands surrounded by narrow darker cracks
Qz2: Light grey quartz with the same grey level as the channels in Qz1. Occasionally with oscillatory zoning.
Qz3: Dark grey diffuse channels intersecting Qz1 and Qz2.
Qz4: Black to very dark grey luminescence.
For more details see Table 4.
Qz1 represents relic high grade quartz forming during upper amphibolite facies metamorphism.

The cracked texture in Qz1 is linked to introduction of aqueous fluids to a dry protolith causing brecciation, dissolution and precipitation of Qz2. Ti in quartz geothermometry (Wark et al.(2006) suggest Qz2 formation at c. 626°C. Repetitive pulses of fluids during uplift facilitated quartz recrystallisation and formation of Qz3. Qz3 is more ductile than Qz1 and Qz2 during exhumation and experienced subgrain rotation and recrystallisation (SGR) whereas Qz1 and Qz2 were brittle.

Trace element analyses documents that quartz was purified through retrograde recrystallisation and Qz3 comprises economically attractive high purity quartz (Sørensen and Larsen, 2007).

Table 3: Alteration types in amphibolites. From Sørensen, Larsen and Austrheim (2007, paper 3). See text for discussion.

Alt1: Potassic alteration with biotite stable
Alt1a: Alteration of amphiboles associated with introduction of biotite. Amphibole cores are dark brownish green whereas rims vary from dark bluish green (Amp3a) through light green (Amp3) to almost colourless (Amp4). **Alt1b:** Veins with a central assemblage comprising plagioclase, calcite, apatite, pyrrhotite, ilmenite/rutile and magnesiohornblende (Amp3). Surrounded by two successive alteration zones, the inner zone comprising amphibole, plagioclase and rutile/ilmenite and the outer zone comprising biotite, plagioclase and ilmenite/rutile. **Alt1c**: En-echelon quartz veins intersecting the foliation in the amphibolite, which comprises both biotite, amphibole and plagioclase Biotite-amphibole plagioclase-ilmenite-(pyrrhotite) bearing reaction zones around en echelon quartz veins **Alt1d**: biotite amphibole rock. Titanite most common, but ilmenite preserved as cores together with rutile. Similar to the alteration around the en-echelon quartz veins
Alt2: Potassic alteration K-feldspar replacing plagioclase and biotite
Replacement of biotite by K-feldspar. Final alteration product is a light grey rock consisting of K-feldspar, and light green amphibole (amp4). Titanite is very abundant in this rock type and almost no ilmenite/rutile is observed. Several types of replacements are seen replacing Alt1 assemblages
Alt3: scapolitisation
Massive scapolitisation. Quartz veins surrounded by reaction rims of scapolite, but minor amounts of scapolite are also observed in many places in the amphibolite. The Quartz veins with the reaction rim of scapolite have a different colouration than quartz veins with less scapolite. The scapolite has a white colour and is only distinguished from commonly occurring white feldspars by its characteristic cleavage

Table 4: Quartz types in the study area. From Sørensen and Larsen (2007, paper 1). See illustration in Figure 4

Quartz type	SEM-CL texture	Genetic interpretation
Qz1	Bright islands surrounded by darker cracks. Typically partially luminescence quenched.	Relic high grade quartz. The island texture testifies to a brecciation and dissolution process and to the formation of Qz2. This related to sudden influx of hydrous fluids under stress in dry protolith quartz.
Qz2	Light grey, sometimes with weak oscillatory zoning. Brighter cores and darker rims, approaching the luminescence of type 3.	Relates to brecciation and dissolution/re-precipitation of Qz1 and to the first observed influx of hydrous fluids. Qz2 also relate to thrust related dynamic recrystallisation involving high temperature grain boundary migration (GBM) in relation to trusting. Dynamic recrystallisation in Qz2 occur together with plastic deformation of feldspar
Qz3	Dark grey diffuse fluid channel texture, which follow grain boundaries or cut through grains. Qz3 is commonly in optical continuity with Qz2, but is distinguished by the absence of rutile needles and by the SEM-texture.	Relates to influx of aqueous fluids and to SGR (sub grain rotation recrystallisation) in relation to thrusting, which occur only in Qz3 and in not in juxtaposed Qz2 and Qz1 which commonly show evidence of brittle deformation at the same time that Qz3 deform plastically. This is inferred to reflect local variations in the H_2O fugacity. Also associated with breakdown of rutile to titanite.
Qtz4	Narrow cracks and pods of black quartz, crosscutting the other types.	Mostly dissolution textures, comprising two types of cracks: 1: Interconnected network of non-luminescent quartz, following micron thin irregular trans/circum-granular cracks. Texture suggests that pure dissolution was dominant and Qz4 thus probably formed in the retrograde dissolution field of quartz. 2: Straight trans-granular cracks intersecting the irregular cracks.

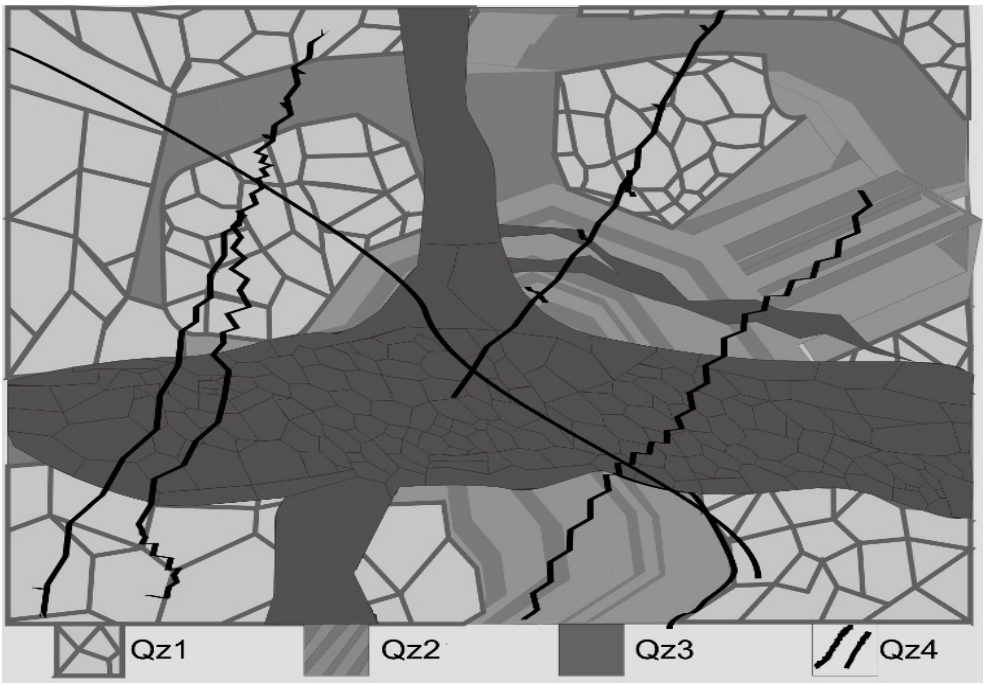

Figure 4: Quartz types as defined by optical microscopy and SEM-CL. See Table 4 for description.

4 Analytical methods

4.1 Microthermometry

Fluid inclusion microthermometry was accomplished with a Linkam THMSG600 fluid inclusion stage (Linkam Scientific instruments Ltd.), mounted on a Nikon E600 optical microscope equipped with long distance lenses facilitating magnification to 1000x and a PIXELLINK PL-A662 firewire digital camera. Images and videos were recorded along with the microthermometric experiments on a computer using the Linksys32-DV software (Linkam Scientific instruments Ltd.).

Meting behaviour was studied after cooling to -100 -196°C, followed by heating. Inclusions with simple phase behaviour were measured "live", using the manual controls in the Linkam software. Phase transition were first estimated using a high heating rate (20-10°C/min) and then refined using slower heating rates (1-2 °C/min) after keeping the temperature just below the phase transition temperature for 1 or 2 minutes. More complex inclusions were first estimated manually according to the above procedure. Then results were refined using video recording during slow heating experiments. Phase changes that were not observed manually during slow heating were

then detected by carefully inspecting the recorded video. This method was particularly strong in estimating eutectic melting temperatures that otherwise may be hard to distinguish from recrystallisation

Phase transitions during heating from 20^{o}C, comprising LV-L, LVS-LS; LS-L and LVS-LV, were recorded live, using heating rate of 2°C/min near the transition temperature after the temperature was kept constant for a while. Experiments with slower heating rates confirmed the observed phase transition temperatures.

The fluid inclusion stage was calibrated with a set of synthetic fluid inclusions (fluids Inc.) with 10 measurements on each standard. CO_2 was used for calibration at -56.5°C, an NaCl (25 wt%) was used for calibration at -21.1°C, the eutectic point in the H_2O-NaCl binary, a NaCl (10wt%) standard was used for calibration at –6.646°C. A regression line through the calibration point was strictly linear consistent with a low 0 point offset (- 0.0027 = 0.0) and temperature offset at Tm_CO_2 of -0.91°C. This calibration procedure was far superior of methods using solid standards that failed to give consistent results. However, powder standards were used for high temperature calibration to avoid the subtle volume changes associated with synthetic inclusions.

4.2 Volume fraction estimates

Volume fractions were estimated in a multistage procedure. The bulk inclusion volume was estimated by multiplying the depth (z-axis) of the inclusion with the cross section area (x-, y-axis) of the fluid inclusion. This approach gave good results for regularly shaped inclusions whereas irregularly shaped inclusions gave more uncertain estimates. Relative phase volumes inside the inclusions are now easily obtained, because the phases inside the inclusion have simple shapes. Bubbles of liquid or vapour phases are estimated by measuring two radii and calculating the volume of an ellipsoid body. This ignores the effect of occasional squeezing of the liquid/vapour bubbles against the upper wall of the inclusion. Solids occurring in simple forms were also estimated using simple geometric equations. Phases occupying the rest of the inclusion are calculated by subtraction from the previous volume estimates.

5 Fluid types and textures

5.1 Strategy

Four generations of fluid inclusions are covered by this study: FIA1, FIA2, FIA3 and FIA4.

To establish the fluid chronology, we used the textural chronology of quartz established by Sørensen & Larsen (paper 1, 2007) (Table 4, Figure 4) together with the alteration types in amphibolite and calcsilicates (Table 4). A more detailed discussion on the quartz evolution is found in paper 1 and a discussion of the metasomatic alteration of amphibolite is found in paper 3.

Samples were collected from three localities: 1: locality representative of the prograde amphibolite evolution, 2: representative of retrograde evolution of calcsilicates, amphibolite, quartz veins and quartz-biotite-tourmaline gneisses and 3: Potassic alteration in relation to en-echelon quartz veins intersecting amphibolite (see Figure 1on page 4 for locations).

5.2 FIA1: garnet-quartz symplectite in amphibolite

FIA1 comprises isolated primary carbonic inclusions and inclusion clusters in quartz in garnet quartz symplectites and formed simultaneously with the symplectites. The symplectites comprise symplectitic garnet and quartz, with minor ilmenite, Cl-apatite and hastingsite. They occur in lenses enclosed by garnet amphibolite, and are interpreted as minimum melts formed by partial melting of the amphibolites (Figure 5a).

The fluid inclusion hosting quartz is bright luminescent with cracked microstructures, comprising bright islands surrounded by duller luminescent channels (Figure 5b). Accordingly, they classify as Qz1 of Sørensen & Larsen (2007, paper 1) that is interpreted as a high temperature quartz type. The inclusions are dark pure liquid inclusions at room temperature (Figure 5c). Similar inclusions are found in Cl-apatite and in zircon in the garnet quartz symplectites. FIA1 co-existed with the partial melts forming the garnet quartz symplectites, but probably experienced post entrapment modification due to fracturing of the host quartz grains.

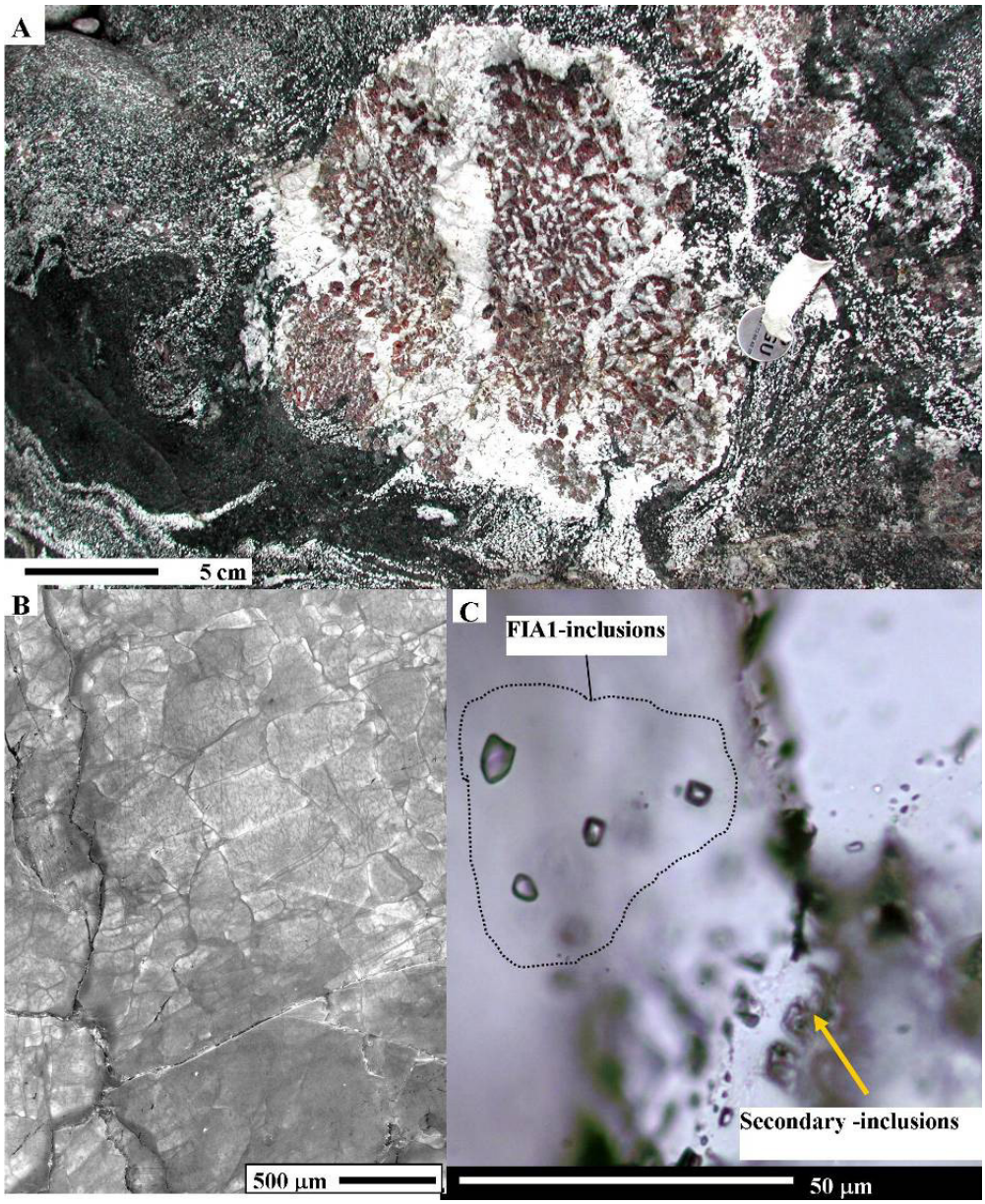

Figure 5: Occurrence of FIA1 in garnet quartz symplectites. A) Field picture of garnet quartz symplectite, intersecting garnet amphibolite. B) The cracked texture of the quartz (Qz1) containing inclusion belonging to FIA1. C) Typical cluster of FIA1 carbonic inclusions.

5.3 FIA2: CO_2 and H_2O-rich inclusions in en-echelon quartz veins in amphibolite: related to potassic alteration

FIA2 comprises CO_2-rich and H_2O rich primary inclusions in Qz2 (see (Sørensen and Larsen, 2007, paper 1)and Figure 4/Table 4). They occur in amphibolite hosted en echelon quartz veins at locality 3. The veins are bordered by a metasomatic tourmaline, amphibole, biotite, plagioclase and ilmenite alteration zones (Figure 6) comprising decussate amphibole, Biotite and plagioclase (Figure 6). The tourmaline is a black schorl rich dravite-schorl solid solution and exclusively occurs in dm-thick layers next to the quartz vein. This is followed by first a dm-thick zone rich in biotite and then a dm-thick zone rich in plagioclase and amphibole. The quartz vein quartz is mostly Qz2, however Qz 1 relics are also common. Both Qz1 and Qz2 are intersected by a network of micron-thick cracks of Qz4 (Figure 6d). The quartz vein is deformed and primary inclusions are rare amongst numerous trails of secondary inclusions.

However, primary inclusions comprising H_2O-rich brines and CO_2-H_2O low saline compositions, were positively identified in growth zones in Qz2 (Figure 6d). At room temperature the H_2O-rich inclusions comprise liquid water and a liquid CO_2 phase comprising 5 vol%. The CO_2-rich low salinity inclusions comprise liquid H_2O, liquid CO_2 and CO_2 vapour at room temperature (Figure 6d), with variable phase volume proportions (see microthermometry results page 29).

The growth zone related inclusions are intersected by Qz4 filled cracks with secondary inclusions and modified primary inclusions. The biotite-amphibole alteration assemblage surrounding the quartz veins is a common assemblage and related to fluid related amphibole alteration, formed during exhumation (Sørensen et al., 2007, Table 3).

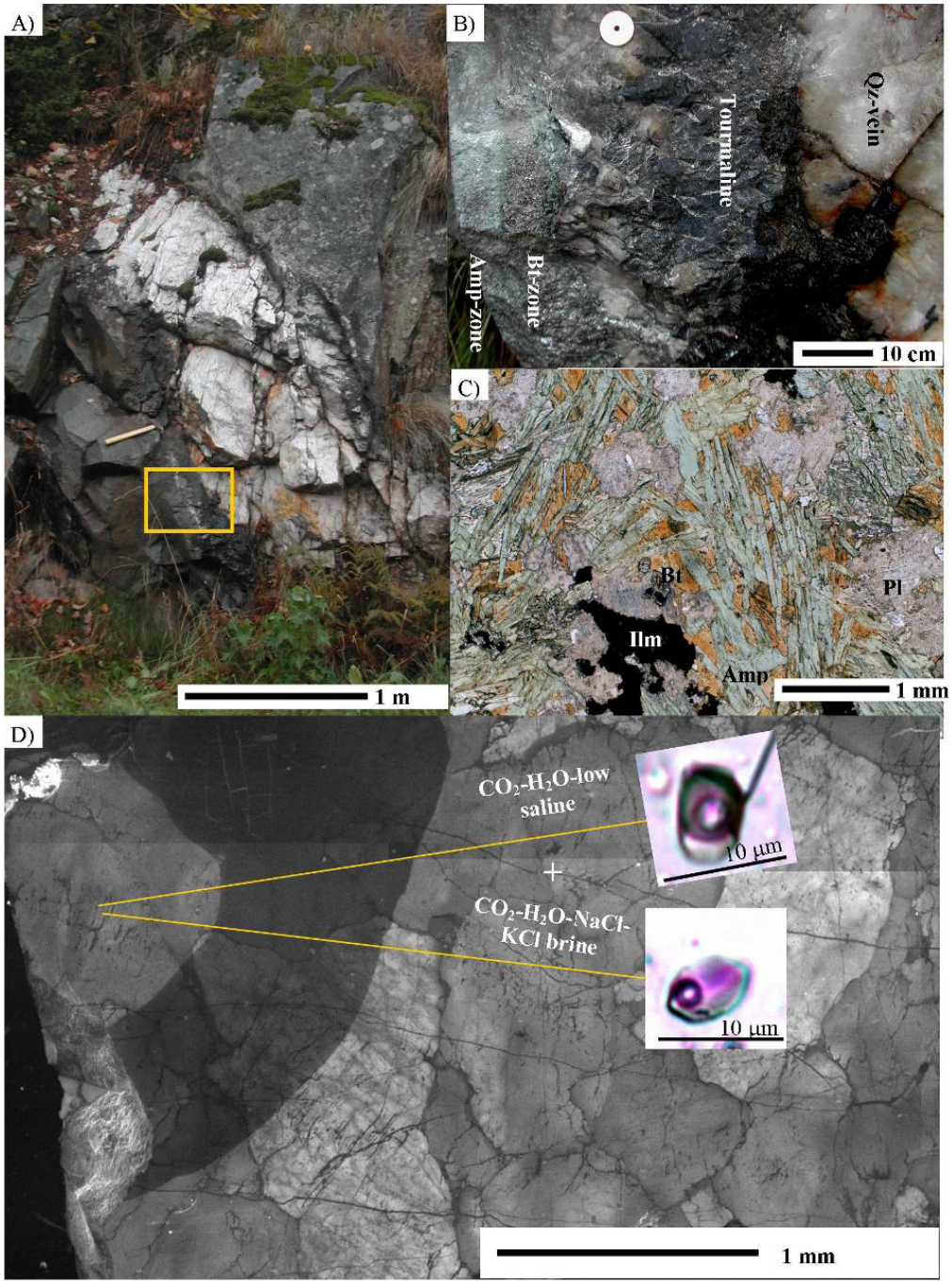

Figure 6: Textures associated with FIA2 inclusions. A) Field image of en-echelon quartz vein intersecting amphibolite. B) Zoom on contact between quartz vein and amphibolite

showing alternating dm-tick layers in the host rock alteration zones. C) Typical alteration assemblage, comprising amphibole, biotite plagioclase and ilmenite. D) SEM-CL texture of quartz in the vein comprising relic Qz1 grain and Qz2, which are both intersected by micron thick cracks with Qz4. Also shown is typical fluid inclusions in Qz2, comprising a mixture of H_2O-rich H_2O-CO_2-NaCl-KCl brines and CO2-rich low salinity H_2O-CO_2-salt inclusions.

5.4 FIA3: LVS primary inclusions in recrystallised quartz, related to scapolitisation and rutile breakdown

FIA3 occurs in recrystallised quartz forming a network of mm-thick fluid channels. These channels correspond to Qz3 of paper1 (see Figure 4and Table 4). They are observed in two settings:

1: FIA3 is associated with Bleaching zones in quartz-biotite-tourmaline gneiss (Figure 7a) causing alteration of biotite to muscovite and chlorite and recrystallisation and bleaching of blue quartz to colourless quartz. Biotite follows the foliation of the non –bleached biotite quartz gneiss, and is intersected by the bleaching zones (Figure 7a). Quartz in the non-bleached quartz biotite mainly comprising Qz1 and Qz2. Qz1 comprises chessboard subgrain microstructures, which suggests that they were deformed at high temperatures. The chessboard subgrain pattern is partly overprinted by prismatic subgrains that formed at lower temperatures. Qz2 grains do not show chessboard textures hence must have formed after the initial deformation of the Qz1 grains. On the contrary, deformation lamellae in Qz2 may very well be synchronous with prismatic subgrain formation in Qz1. Similar observations were confirmed by Sørensen & Larsen (2006, paper1) in quartz veins from the same locality. Accordingly, Qz1 and Qz2 could be distinguished by common optical microscopy. Qz3 on the contrary, had to be identified by SEM-CL. However, in thick sections (100 μm), Qz3 may be recognised by the absence of rutile needles, which are common in Qz2. (see below). This difference is not as easily observed in normal thin sections.

Inclusions follow broad channels of Qz3, intersecting Qz1 and Qz2 (Figure 7b and c). The broad channels with Qz 3 are intersected by a network of micron thick cracks with Qz4 (Figure 7b) and calcite bearing fluid inclusions. Qz3 in the fluid channels is in optical continuity with the host Qz2 grains, but they are differentiated optically by the absence of rutile needles (Figure 7e). These observations suggests that rutile was destabilised in relation to the influx of FIA3 fluids and is confirmed by the breakdown of rutile to titanite in relation to luminescence quenching textures comprising Qz3 and Qz4 (Figure 7d). The absence of calcite in the vicinity of rutile grains infer that calcium required for titanite replacement of rutile was supplied by a fluid phase.

As with the quartz scapolite veins, fluid inclusions in Qz3 infiltrate along channels of dull Qz3 intersecting Qz1 and Qz2.

Because FIA3/Qz3 textures are intersected by Qz4 with carbonic mineral inclusions, it is inferred that the fluid evolved to more Ca-rich compositions, facilitating calcite precipitation. In addition the FIA4 texture indicates that quartz was dissolved and not precipitated during this stage.

Qz3 textures similar to those observed in this study are also found in quartzites where they relate to hydrolytic weakening and localised increased recovery rate and subgrain rotation recrystallisation associated with thrust-related shear deformation (paper 1, Sørensen and Larsen, 2007) and imply that Qz3 formed during exhumation.

2: FIA3 is also associated with quartz in quartz scapolite veins, related to scapolitisation of plagioclase in amphibolite. Veins are composed of a cm-thick rim of scapolite followed by a cm-thick central zone of quartz (Figure 8). The Cl-intensity of the quartz is generally low and is classified as Qz3 and 4. However, in detailed SEM-CL studies a complex fluid migration network is revealed. A broad Qz3 zone is intersected by a micro-thick network of Qz4, comprising micro-inclusions of calcite and calcite bearing fluid inclusions. Qz3 may either be classified as unevenly luminescent and partly recrystallised comprising fluid migration channels or more evenly dull luminescent newly formed Qz3 grains (*new Qz3*). The new Qz3 grains either occur as inclusions in scapolite grains or in rims enveloping scapolite grains (Figure 8). Fluid inclusions related to Qz3 occur in intragranular trails associated with duller channels. Fluid inclusions are rare in the new Qz3 and were not large enough for microthermometry.

Two generations of later fluid inclusions intersects FIA3. The oldest generation is $LVS_1(S_2)$ inclusions following the Qz4 network (Figure 8). They carry liquid H_2O, vapour, halite (S_1) and commonly also calcite (S_2) (Figure 8). They are fairly similar to FIA3 inclusions but may be differentiated by their direct association with Qz4, restriction to narrow fluid inclusions trails and by the presence of calcite (Figure 8). They are not included in this study because they failed to freeze during microthermometry. However, similar sizes of the halite cubes and the calcite daughter minerals imply an increase in the Ca-content in the fluid phase when going from fluids in Qz3 to fluids in Qz4.

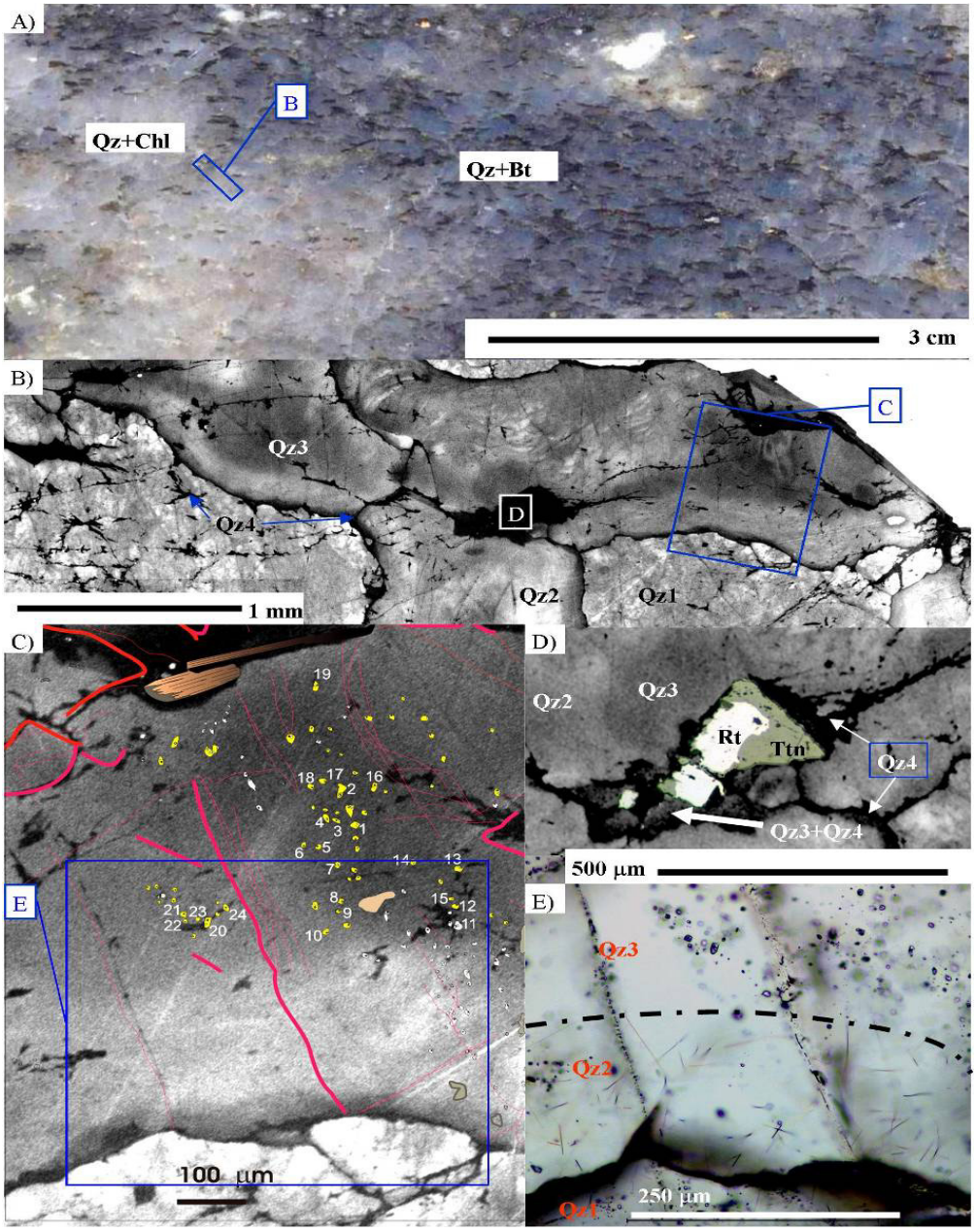

Figure 7: Textural relation with respect to FIA3 in quartz biotite gneiss. A) Field image showing bleaching of the gneiss in relation to fluid infiltration. Bleaching is an effect of both a colour change in quartz from blue to colourless and due to the breakdown of biotite to chlorite and muscovite. B) SEM-CL image showing the textural relations involving Qz1, Qz2, Qz3 and Qz4. Qz3 follows broad luminescence quenching channels,

intersecting Qz2. C) Zoom on B showing the relation between FIA3 fluid inclusions (yellow) and Qz3 luminescence quenching textures. D) Titanite replacing rutile in relation to luminescence quenching textures. E) Optical image showing the presence of rutile needles in Qz2 and their absence in Qz3.

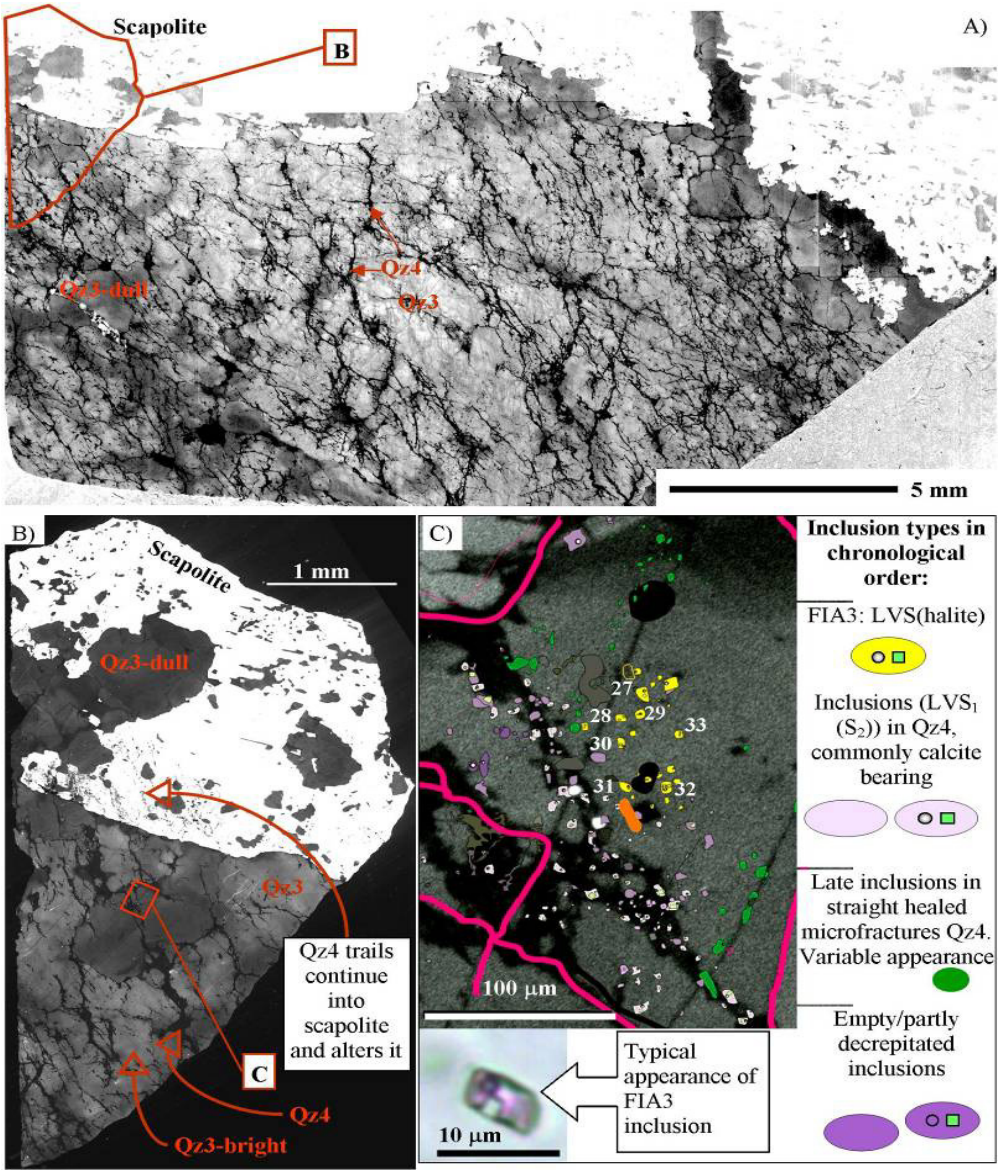

Figure 8: SEM-CL/optical textures in relation to FIA3. A) Overview showing the relations between Qz3, Qz4 and scapolite. Contrast is enhanced such that differences with quartz

type Qz3 are seen. Qz3 divides into three groups: #1: Bright unevenly luminescent grains, 2: dull channels intersecting #1, #3: new grains of Qz3 commonly as inclusions or next to scapolite. B) Detail from (A) showing the location of the fluid inclusions in (C). Note that Qz4 textures intersect scapolite, documenting that Qz4 formed after scapolitisation. C) Detailed view showing the relation between fluid inclusion assemblages and SEM-CL textures. Inclusions later than FIA3 are distinguished by a combination of optical microscopy and SEM-CL.

5.5 FIA4: LV primary fluid inclusions in calcite and epidote in epidote-actinolite-calcite-pyrite vug fillings.

FIA4 comprise LV inclusions in calcite and epidote in a tremolite-epidote-pyrite-calcite-flour-apophyllite assemblage comprising vug fillings at the boundary between the quartz-biotite-plagioclase-tourmaline gneiss and the diopside rich calcsilicate rocks. The vugs comprise an outer zone of mint green tremolite, followed by a cm-thin rim of epidote and pyrite (Figure 9). Calcite is intergranular between epidote and tremolite and also occurs together with flour apophyllite in the central part of the vugs (Figure 9). Epidote is only present together with pyrite (Figure 9). This together with the observation of pyrrhotite relics together with pyrite suggests that excess iron from the alteration of pyrrhotite to pyrite supplied Fe for epidote formation. The epidote-calcite-tremolite-apophyllite assemblage probably formed from the breakdown of a metastable diopside-tremolite-pyrrhotite-phlogopite assemblage, where SiO_2 and Al_2O_3 were supplied from the neighbouring gneiss unit.

Fluid inclusions occur in growth zoned calcite. Epidote grains are zoned with increased pistacite content at their rims and along fractures (Figure 9). Fluid Inclusions are also common in epidote cores but not in the rims.

Tremolite grains alter to more Fe-rich compositions (into the actinolite field) along rims and fractures (Figure 10). Along with the increased Fe-content in the amphibole the Al content also drops.

The vug-assemblage is part of a complex alteration sequence observed in calcsilicates comprising clinopyroxene (diopside-(hedenbergite)), phlogopite, tremolitic amphibole, epidote, and titanite. The textural relations are summarised in section below.

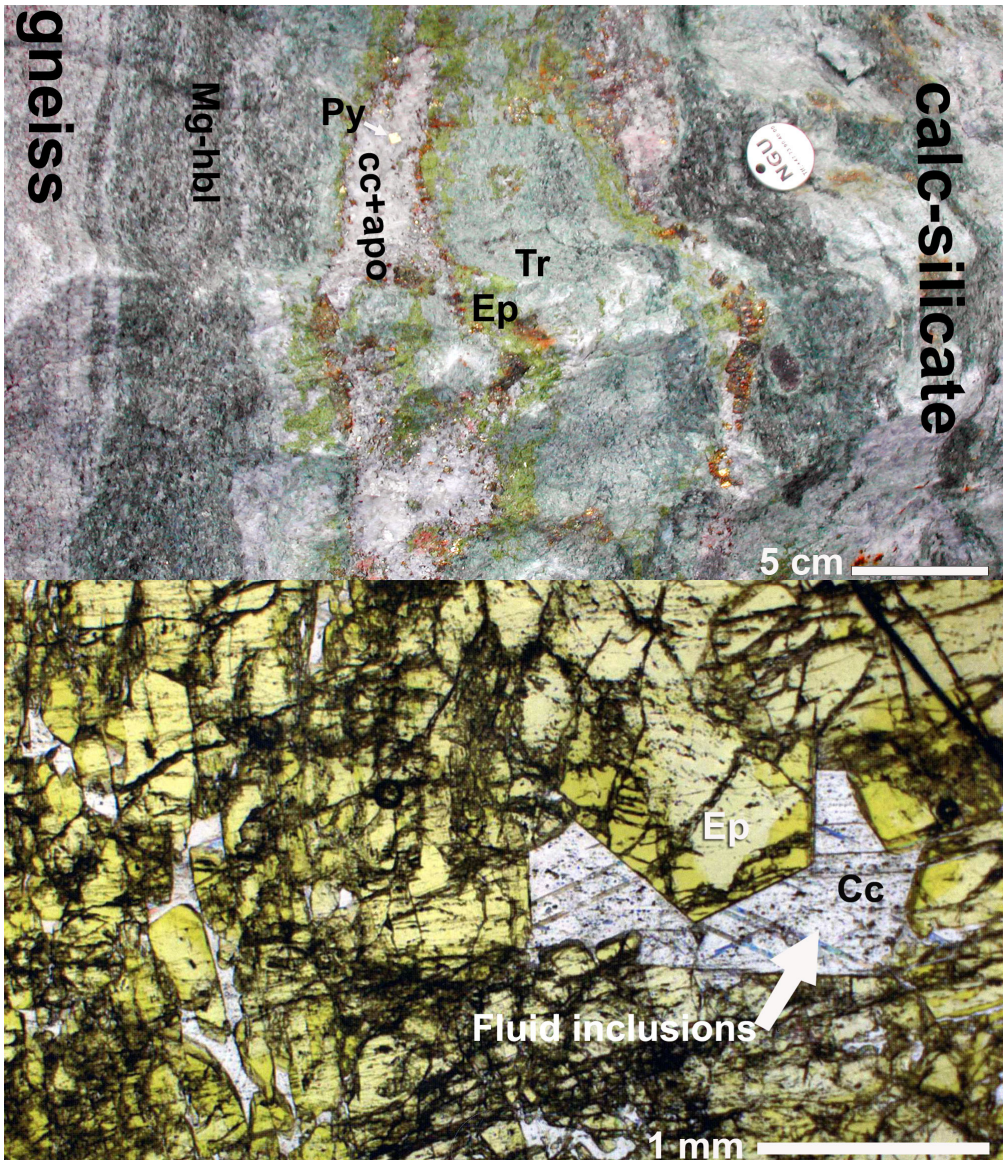

Figure 9: A) Field relations of the tremolite (Tr) - epidote (Ep) – calcite (Cc) - apophyllite (Apo)- pyrite (Py) assemblage (Mp5). The Mp5 assemblage is squeezed in between the calcsilicates and the gneiss unit. B). Thick section (100μm) image showing epidote calcite assemblage. Large calcite grain contains the primary fluid inclusions included in this study. Note the colour variation in epidote with more intensely coloured rims comprising more Fe-rich epidote.

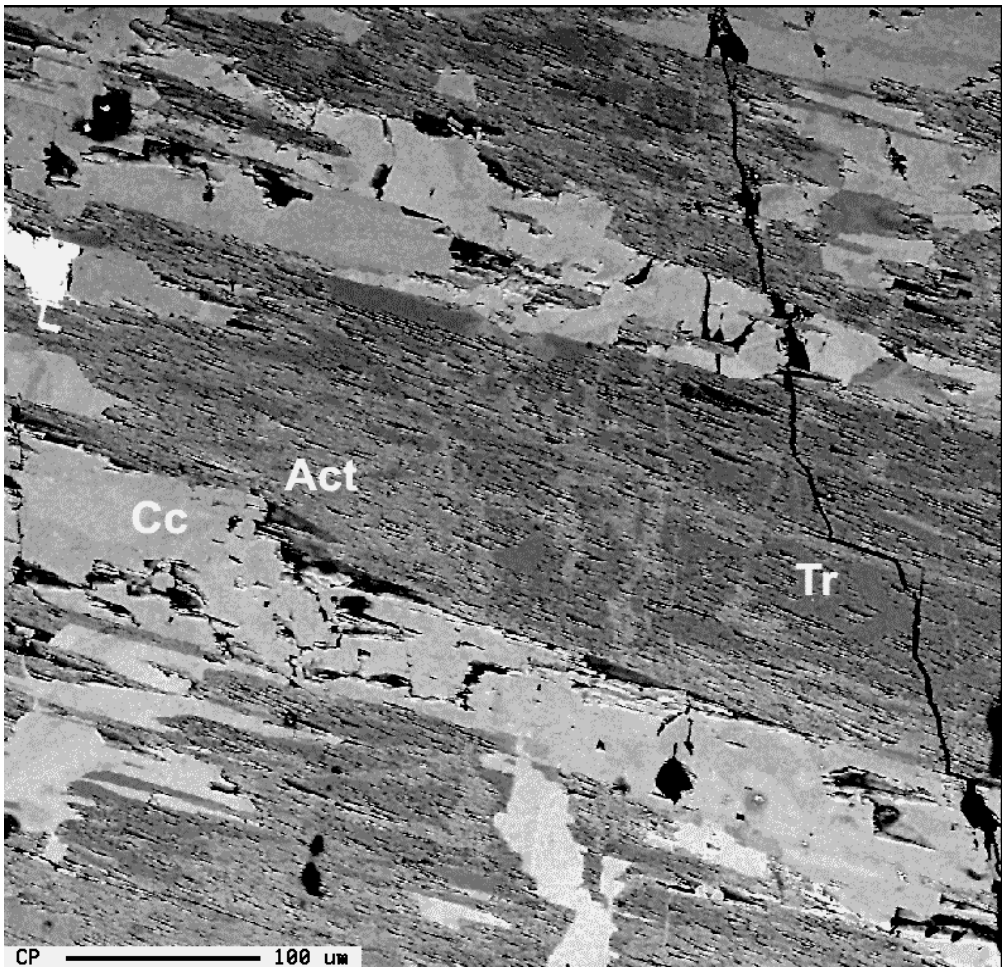

Figure 10: Electron backscatter image displaying calcite (light grey) and amphibole (darker grey). Tremolite (Tr) is altered to actinolite (Act) along fractures.

6 Micro-thermometry results

Most fluid inclusion data were modelled using the FLUIDS1 program suite (Bakker, 2003). However, some inclusion types lack appropriate EOS hence were interpreted with published phase diagrams and extrapolation of EOS expressions.

6.1 FIA1

First melting of the carbonic inclusions occurs at -56.5 to -59 °C, as SV→LV and total homogenisation as LV→L at variable temperatures. H3 phase behaviour(Van den Kerkhof and Thiery, 2001) was followed during heating. This together with the narrow range of meting temperatures implies that the fluids are almost pure CO_2.

The LV→L homogenisation of the inclusions is scattered from -3.7 to 27.2 °C altogether implying post entrapment modifications as it was also implied by the cracked CL-texture of the host quartz grains. H_2O-is absent, however, preferential H_2O leakage can not be excluded (Bakker and Jansen, 1990; Bakker and Jansen, 1994).

Accordingly, the only information available from FIA1 is that CO_2 was the stable carbonic phase during the formation of the garnet quartz symplectites.

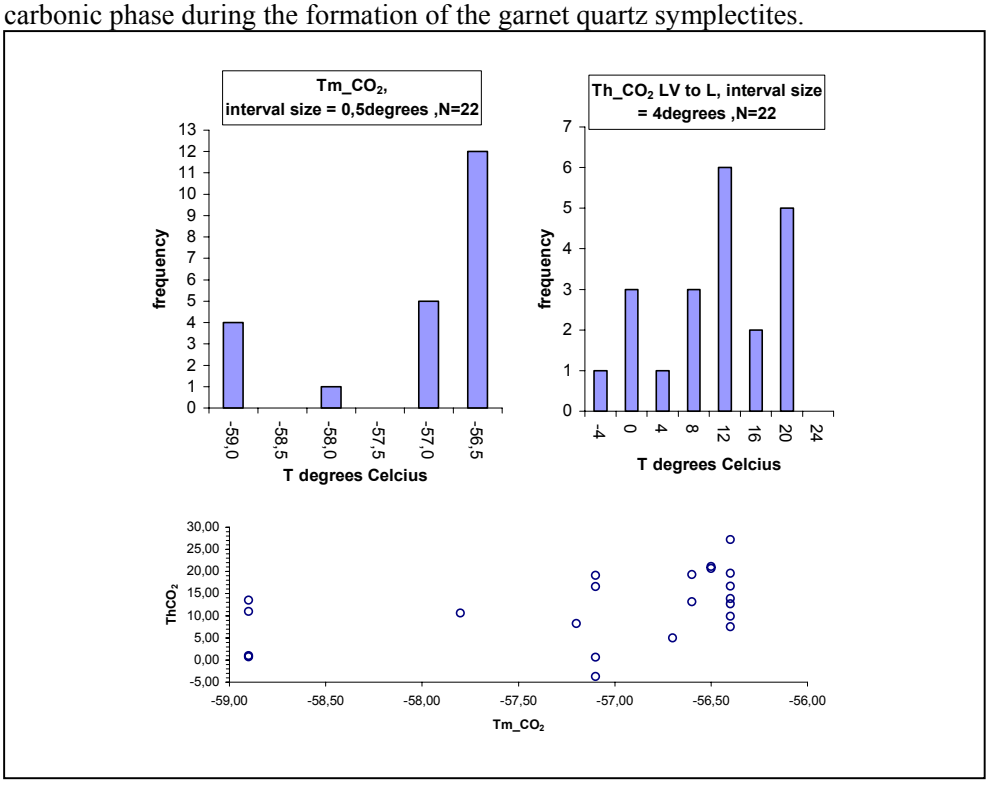

Figure 11: FIA1 microthermometry data. Upper left Tm_CO_2 displaying a narrow temperature range. Upper right: homogenisation LV→L (Th_CO_2) showing a wide range of temperatures. Lower diagram show a plot of Th_CO_2 vs. Tm_CO_2 showing that there is no correlation.

6.2 FIA2

The FIA2 comprises two groups i.e. CO_2-rich and H_2O- rich inclusion, which together with textural features imply immiscible fluids. Volume fraction estimates of the CO_2 rich inclusions show a large scatter (Figure 12). However, the H_2O rich inclusions have a narrow range in volume fraction estimates with 95 % L_{H2O} (+ CO_2 dissolved in the H_2O phase) and 5 % CO_2 (Figure 12).

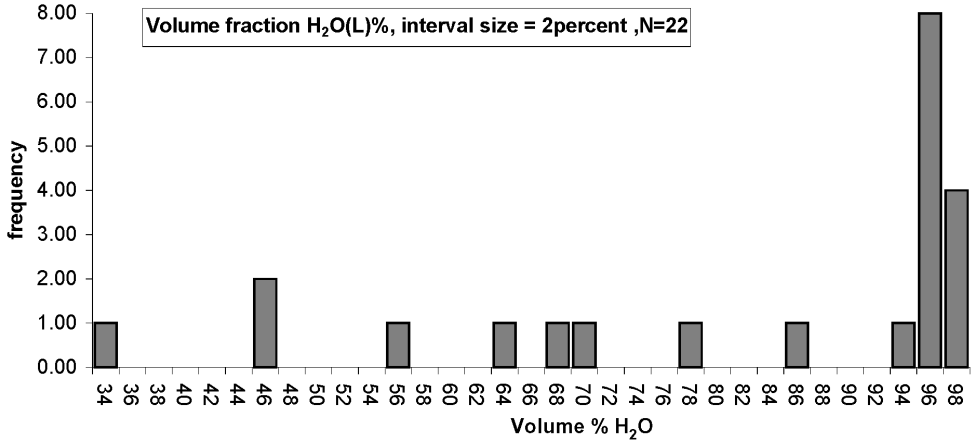

Figure 12: Volume fraction estimates showing that only the H_2O-rich inclusions have constant volume fractions and that the CO_2-rich inclusion underwent post-entrapment modifications.

The melting behaviour of the carbonic phase is SG→LG at temperatures close to the melting temperature of pure CO_2 (Figure 13). The clathrate melting temperature is -11 to -2 °C for the H_2O rich inclusion, whereas it is approximately 8 °C for the CO_2-rich inclusions (Figure 13). Both groups fall in narrow ranges of clathrate melting temperatures hence implying that the aqueous phase salinity remained constant. First melting of the aqueous phase could only be determined in the H_2O-rich inclusions and consistently fall at -24.7 °C, i.e. close to eutectic minimum of the H_2O-NaCl-KCl ternary system. The slight offset is probably caused by the presence of CO_2 which is known to systematically lower melting temperatures in aqueous electrolyte inclusions (e.g. Hedenquist and Henley, 1985). This together with the biotite bearing alteration assemblage indicates that the aqueous liquids are best defined by the H_2O-NaCl-KCl ternary system.

Th-total of the H_2O-rich inclusions is about 200°C. The salinity estimates obtained from clathrate melting and melting of ice and hydrohalite show that the salinity was close to the eutectic point i.e X_{NaCl} = 20.2 wt%, X_{KCl} = 5.8wt%. Therefore, the coexisting immiscible fluids probably did not form by phase separation because the H_2O-CO_2 solvus at near eutectic salinities occur at a much higher temperature than the observed Th-total of the H_2O rich inclusions. In conclusion, the H_2O and CO_2 rich

inclusions are not co-genetic but were introduced as separate fluids, during the formation of the en echelon quartz veins and quartz type Qz2.

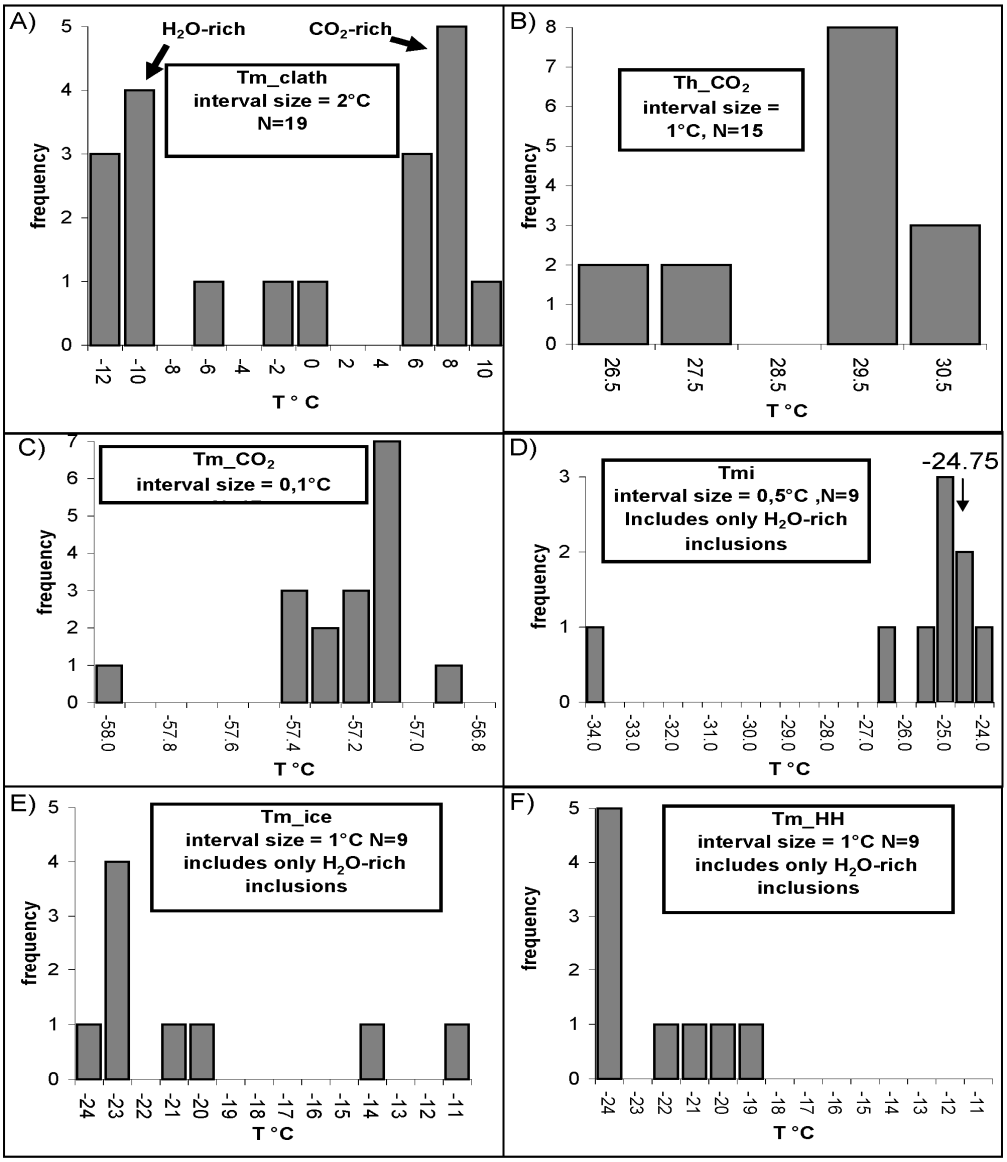

Figure 13: Microthermometry results from FIA2, CO_2-H_2O immiscible fluids. A) Clathrate melting temperatures, not two groups B) Homogenisation of CO_2 C) Tm_CO_2 D) First melting temperatures (Tmi). F) Final melting of hydrohalite (Tm_HH).

6.3 FIA3

FIA3 comprise a narrow range of melting temperatures (Figure 14) with first melting observed at -49 to -45 ºC hence supporting an eutectic point around -52°C, given that the first melt fractions are difficult to observe. Thus it is inferred that the inclusions belong to the NaCl-$CaCl_2$-H_2O system.

Final melting of ice occurs at -27 to -25 ºC with a few outliers around -40°C (Figure 14). Melting of hydrohalite was uncertain and occurs at different temperatures during sequential heating experiments and hence is not included in the measurements. In most inclusions the average LV→L Th occur at 126-128°C before melting of the solid phase (average TmS=150°C). Th and TmS are negatively correlated, in a trend suggesting constant density (Figure 14). Absence of clathrate/hydrate formation implies that H_2O is the only COH fluid.

In the absence of certain hydrohalite measurements, the Ca/Na ratio was estimated from final melting of ice. This introduces errors that are smaller than the error in estimating hydrohalite melting (Williams and Samson, 1990). The salinity and the Ca/Na ratio was estimated with (Vanko et al., 1988; Williams and Samson, 1990) and gave a salinity of 31 wt% with 25 wt% NaCl and 6 wt% $CaCl_2$.

Halite (H) melting generally occurs at higher T than the LV→L phase transition hence differs from the available experimental data where vapour saturated conditions are required during halite melting. In our case the inclusion has left the LVH curve at T1. Because the LH liquidus is inclined in PT space an error in the predicted salinity is introduced together with an error in the density and thus also an offset in the isochore (e.g. Bodnar, 2003). Because the conditions of the liquid phase at LVH→ LH phase transition is fairly well constrained and because of the nearness to vapour saturation the error was ignored. Hence the salinity was used together with the LV→L Th to calculate a fairly well constrained isochoric path with the EOS of Zhang & Frantz (1987).

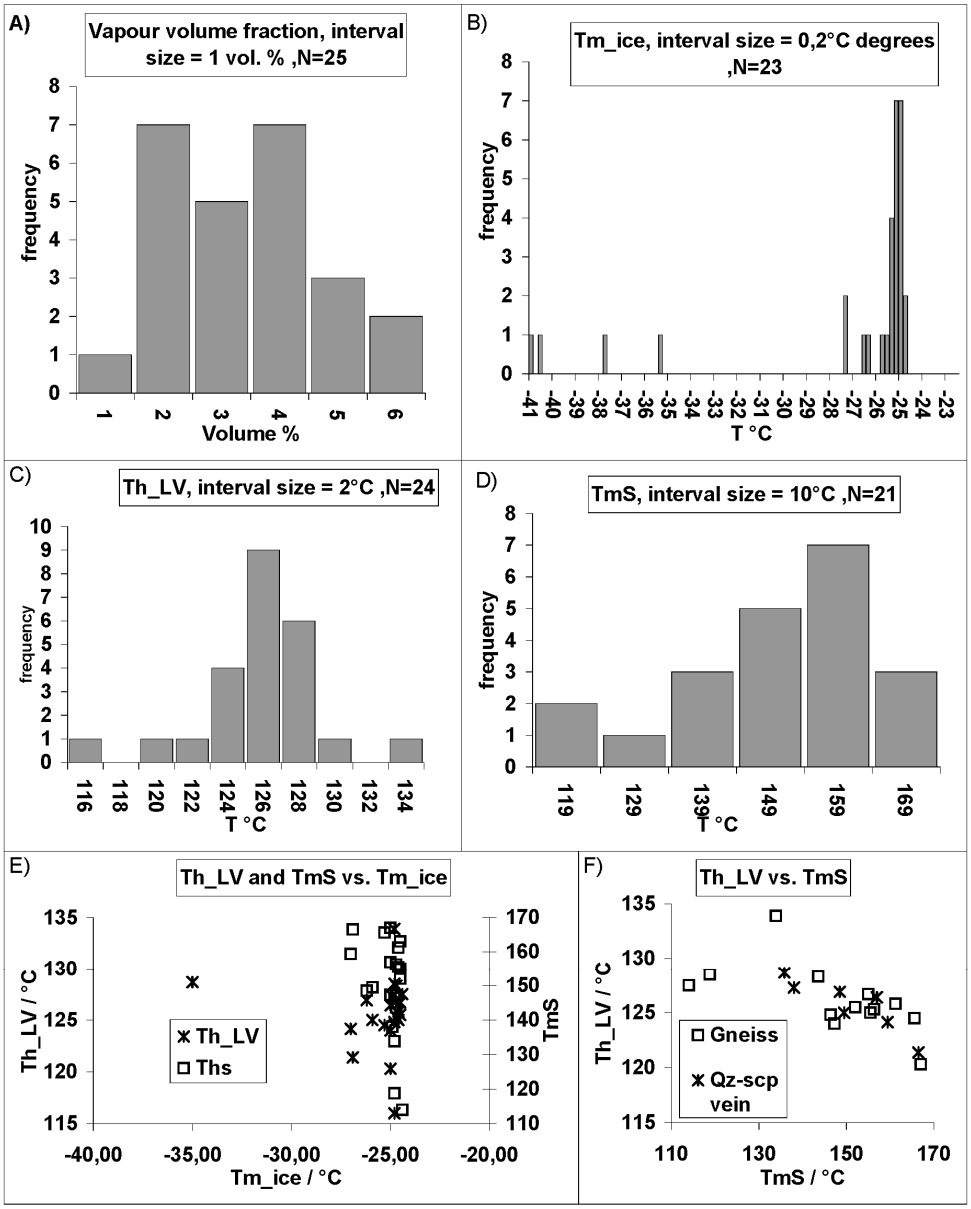

Figure 14: FIA3 microthermometry results. A) Volume fraction estimates B) Tm_ice histogram. C) Th_LV histogram. D) TmS histogram E) TmS and Th_LV showing no correlation vs. Tm_ice. F) Negative correlation between Th_LV and TmS.

6.4 FIA4

FIA4 experienced first melting from -74 to -49 °C and the fluid inclusions with Tmi higher than -60°C featured equilibrium behaviour, characteristic of the $CaCl_2$-NaCl-H_2O ternary system.

Fluid inclusions with very low first melting temperatures, however, show significant melting far below the $CaCl_2$-NaCl-H_2O eutectic point suggesting either metastable behaviour or the presence of other cations (Figure 15). Prior to first melting the inclusions become clouded and then speckled as recrystallisation proceeds during heating. The speckled texture is interpreted as a result of hydrohalite formation (Figure 15). At -70 to -80°C individual grains are recognised (Figure 15). First melting commonly occurs at -65°C and at -60°C liquid comprises a significant proportion of the fluid inclusions (Figure 15). At about -55°C, only one solid phase remains in the inclusions (Figure 15). It appears in lensoid bodies like ice but lye at the bottom of the inclusion and, therefore, are interpreted as antarcticite (Figure 15).

Antarcticite is the last phase to disappear in all fluid inclusions and, therefore, they plot in the narrow antarcticite field in the NaCl-$CaCl_2$-H_2O ternary system. The position of the liquidus in this system is not well constrained hence the antarcticite melting temperatures (Tm_ant) were interpreted in the $CaCl_2$-H_2O binary subsystem from phase diagrams in Crawford (1981).

Antarcticite melting occurs within a wide range from -4 to -43 ºC, with peaks at -37 ºC and -26 ºC (Figure 16). Because of the steepness of the liquid-antarcticite cotectic curve this translates to a narrow salinity range of 31-36 wt % $CaCl_2$ equivalent. Fluid inclusions in epidote cores have a narrow range around -26°C, corresponding to the main peak in calcite hosted fluid inclusions (Figure 16). Similarly the first melting temperatures fall in two clusters; one asymmetrically around -52°C and an other around -65°C. Fluid inclusions in epidote cores are restricted to the narrow range -49 to -51.8°C, suggesting that they are correlated with the inclusions of the -52°C peak of the calcite inclusions (Figure 16). Accordingly, the inclusions with the “normal” first melting temperatures are early and fluid inclusions with the low first melting temperatures are later.

Contoured values of Tm_ant and Tmi, also show a systematic spatial variation (Figure 17). Inclusions with very low first melting temperatures (<-62°C) generally have antarcticite melting temperatures above -30°C (Figure 17). Inclusions with the first melting temperatures above -62°C generally have antarcticite melting temperatures above -30°C (Figure 17). Given the systematic distribution from core to rim of these microthermometric data, it is inferred that the inclusion group with the “normal” first melting temperatures are early and correlates with epidote cores (EpCz70-75) and the fluid inclusions with the low eutectics are younger and relates to the alteration rims on the epidote grains (EpCz65) (Figure 17).

The density of FIA4 is difficult to pin down as no EOS of calcic brines in this salinity and temperature range exist. Therefore, the density of the inclusion bubble was estimated by extrapolating from values of lower salinity solutions calculated with the Krumgalz et al. (1996) EOS, included in the program Bulk from Fluids package

(Bakker, 2003). Results show that the density of the vapour phase is negligible and that the calculated bulk densities follow a strictly linear trend (Table 5) and are used to calculate densities of the 31.7 and 36 wt% inclusions, respectively (Table 5).

Given that an EOS for these conditions is absent we extrapolated from the "low" salinity EOS of Zhang and Frantz (1987) to estimate the isochore (Table 5). The resulting isochors are fit by a linear equation (Table 5).

Table 5: Density estimates by linear extrapolation from lower salinities calculated with bulk and excel. Also shown are slopes and intercepts of calculated isochores.

Calculated with bulk			
D bulk (g/cc)	D vap (g/cc)	Wt% CaCl2	%vap
1.14377	0.000017	22	4.5
1.16315	0.000017	24	4.5
1.182846	0.000017	26	4.5
1.202834	0.000017	28	4.5
1.223085	0.000017	30	4.5
1.230329	0.000017	30.71	4.5
Estimated with linear extrapolation			
D bulk (g/cc)	D vap (g/cc)	Wt% CaCl2	%vap
1.239899309	0.000017	31.7	4.5
1.282677945	0.000017	36	4.5
Linear :			
D(g/cc) = wt%CaCl2*0,0099 + 0,9245, R^2 = 0,9999			
Calculated homogenisation conditions *			
Th_Calc (31.7wt% $CaCl_2$)		126.715 °C	0.450413 MPa
Th_Calc (36 wt% $CaCl_2$)		148.016 °C	0.482372 MPa
Calculated isochores P(bar) = aT(°C) + c **			
	slope(a)	intercept(c)	R^2
31.7 wt% CaCl2	22.67	-2868.56	1
36 wt% CaCl2	22.63	-3344.45	1

*) calculated with Zhang & Frantz 1987 EOS (loner38 (Bakker, 2003))

**) calculated with Zhang & Frantz 1987 EOS included in isoc (Bakker, 2003))

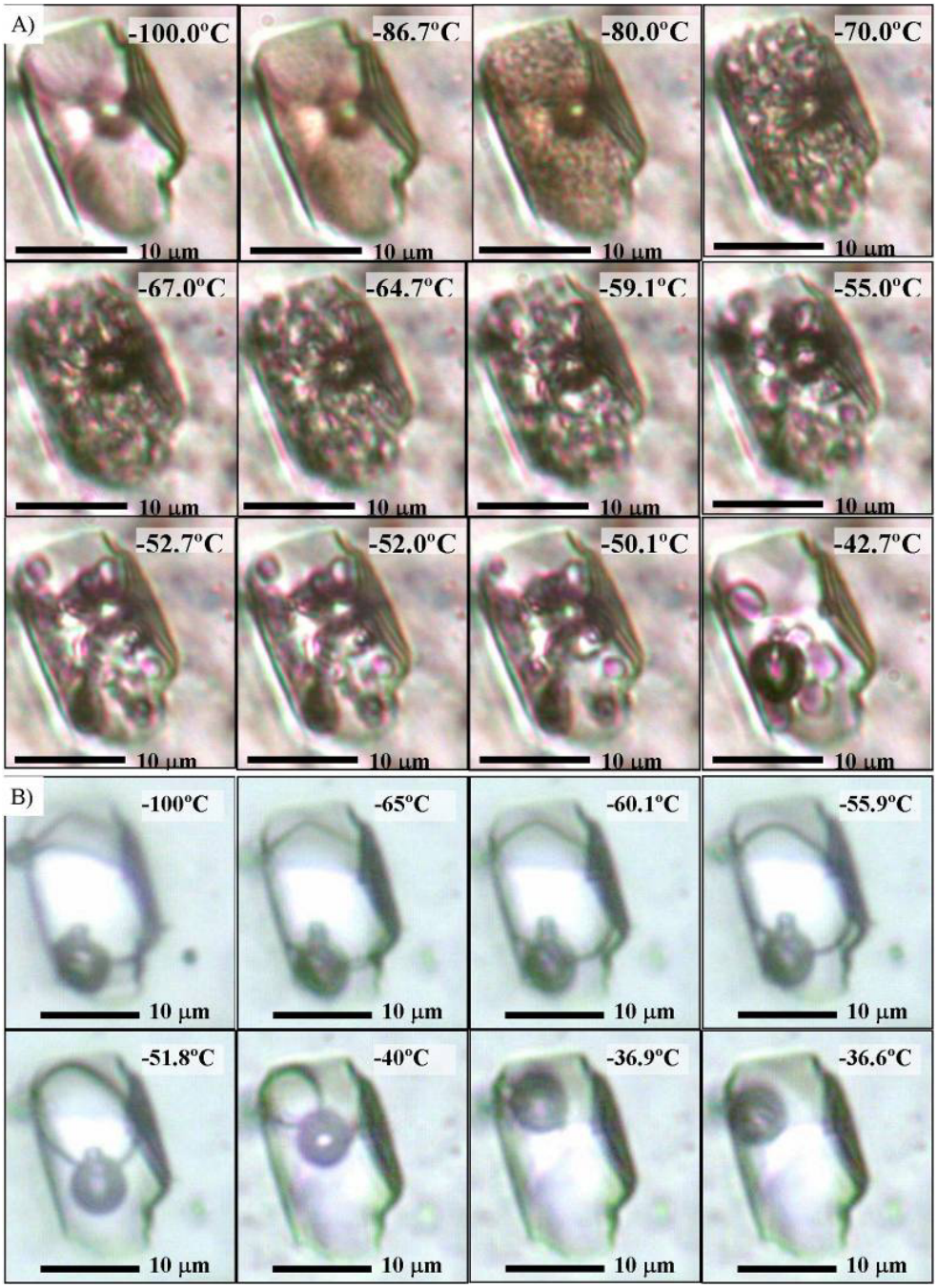

Figure 15: Melting behaviour of inclusions belonging to FIA4 with very low first melting temperature. A) Single cooling and heating path with cooling 20ºC/min. At –100ºC the

inclusion is frozen and glass and relic vapour bubble is observed. During heating the inclusion gradually recrystallises. This is commonly observed around –90 to –85ºC by a darkening of the inclusion and by a speckled appearance caused by tiny crystals of solid phases forming. As heating proceeds the tiny crystals gradually coarsen and at around –70 individual grains are recognised. First melting is difficult to observe but appears around –65ºC, identified by careful video inspection. Around –60ºC the liquid phase becomes clearly visible and near –52 a large proportion of the inclusion is liquid. Two types of solids are seen: one forming relatively large crystals with low relief and tiny crystals of a greenish appearing phase with higher relief/birefringence. At around –50ºC only the low relief persists. This phase continues to melt and at –40ºC only a few crystal remain. These crystals are denser than water as they are situated at the bottom of the inclusion. B) Sequential heating/freezing close to the melting temperature of this phase reduces the number of crystals to 1. During freezing to –100 the crystal adopts a subhedral shape, with a 120 degrees angle between crystallographic surfaces, meeting in a sharp corner. Around –65 this corner roundens, indicating that the crystal melting initiates. As melting proceed the crystal becomes increasingly rounded and has adopted a lensoid shape at about –55.9ºC. At –36.9ºC the solid is almost melted with only a tiny crystal left which finally melts at –36.6ºC.

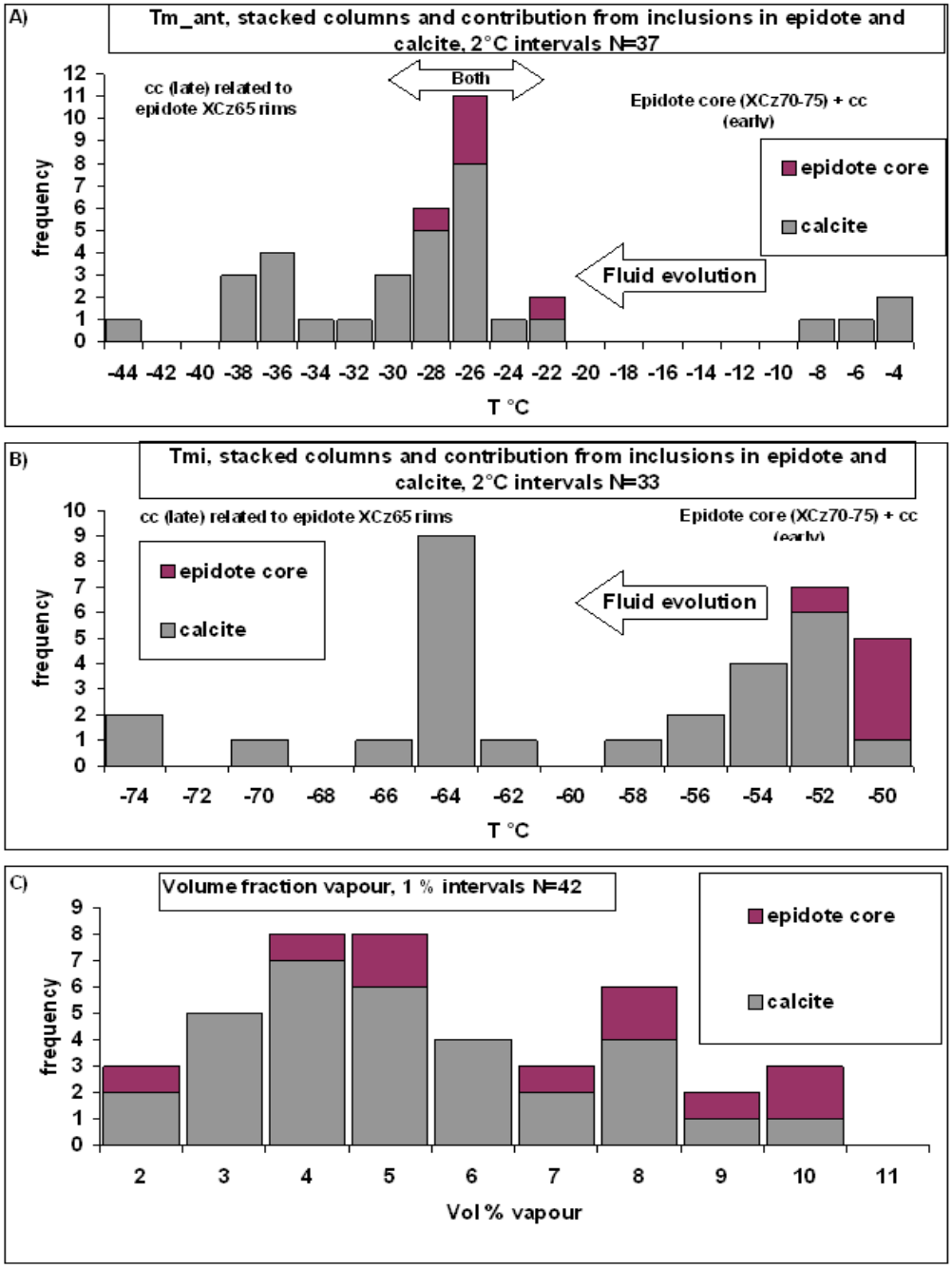

Figure 16: Microthermometry results FIA4. A) Final melting of antarcticite B) First melting C) Volume fraction estimates. Stacked columns of data from epidote and calcite. See text for discussion.

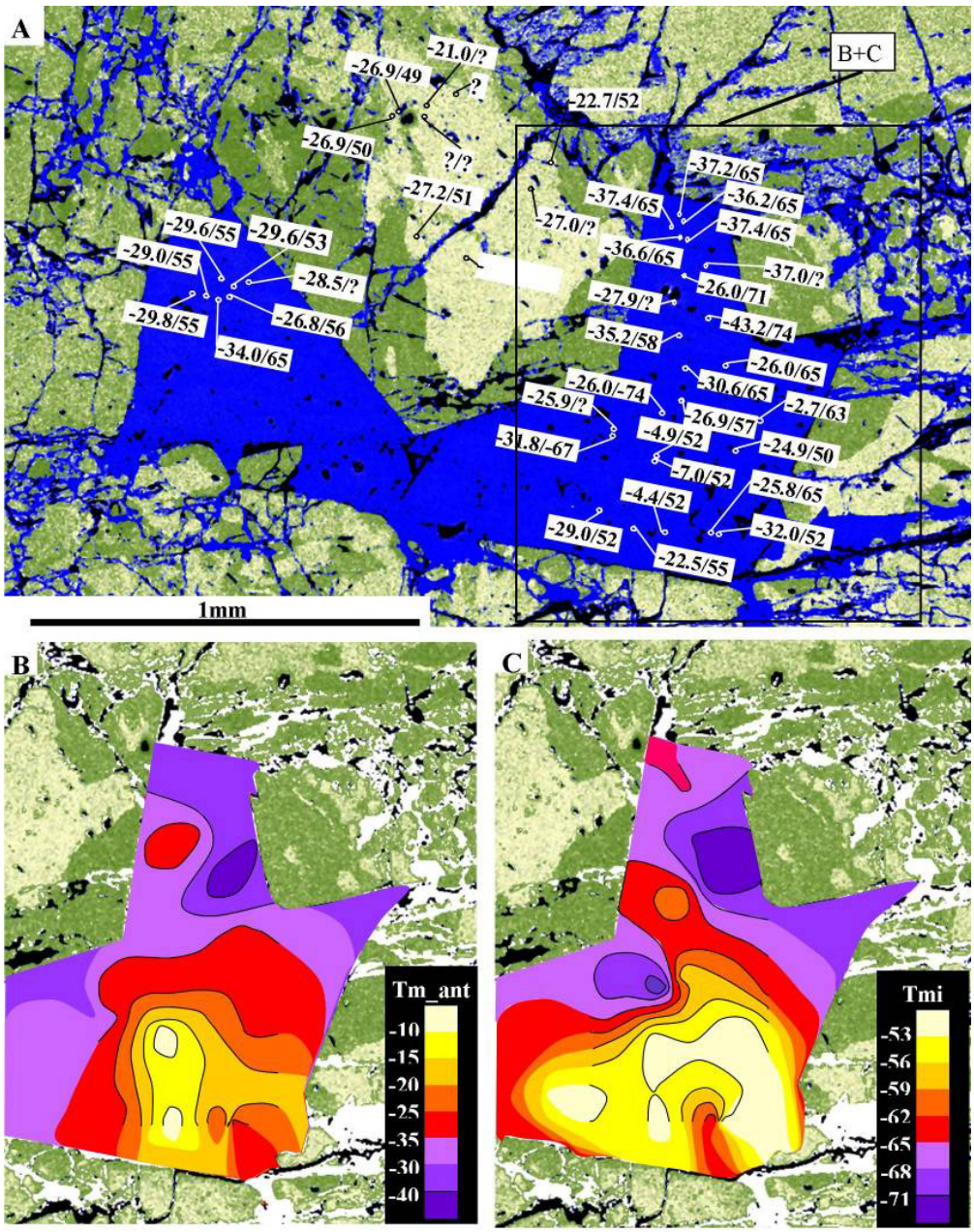

Figure 17: Spatial distribution of antarcticite and initial melting temperatures in inclusions in epidote cz70-75 shown as overlay on colourised BSE image. Blue is calcite, light greenish yellow epidote Xcz =70-75, and green epidote Xcz65. A) Individually plotted values of Tm-antarcticite/Tmi in calcite and epidote cores, note the variable values in

calcite compared to the more constant values in epidote. Note also the increasing abundance of Xcz65 epidote toward the top of the image B) Contour plot with 5ºC intervals of tm-antarcticite. Note the general bottom to top decreasing values and the decreasing values toward epidote cz65. C) Contour plot of Tmi with 3ºC intervals. Note that Tmi decreases toward the top and toward epidote Xcz65. Note also the correspondence between the yellow-red contour of Tm-antarcticite and yellow-orange, indicating a group of inclusions with Tm-antarcticite above –30ºC and Tmi above –62. This group is similar to the inclusions in the epidote cores. Areas with solid lines in the contour plots are contoured based on the fluid inclusion data. Areas that only shaded are inferred.

7 Discussion

7.1 Summary of the observed fluid evolution

FIA1 is texturally correlated with high grade metamorphism of the area and comprise virtually pure CO_2-fluids co-existing with eutectic melts formed by partial melting of amphibolite. In agreement with studies of Fe-Ti oxides in the granulite facies area around Tromøy (Harlov, (2000), CO_2 is the stable carbonic species at the ambient oxygen fugacities.

FIA2 is the earliest retrograde fluid and comprise mixtures of two fluid types: 1) low salinity CO_2-rich H_2O-CO_2 inclusions, 2) H_2O-CO_2-NaCl-KCl brines with near eutectic compositions and low in CO_2. Thermodynamic modelling does not allow type 1 and 2 inclusions to be the result of in situ phase separation. Rather they represent fluid mixing of fluids derived from separate sources.

FIA3 comprise LVS inclusions of aqueous brines and no carbonic fluid. The most important salts are NaCl (average 25 wt %) and $CaCl_2$ (average 6 wt%). The salinity is near constant and LV to L homogenisation occurs in a narrow range around 129 °C Altogether giving dense brines following a steeply inclined isochore.

FIA4 is LV inclusions representing aqueous $CaCl_2$ (31-36 wt%) brines with no carbonic fluids. The degree of fill is high giving dense fluids following a steeply inclined isochore In P-T space. The final melting of antarcticite varies systematically along growth zones in calcite. Epidote grains are zoned with Xcz (71) in cores and Xcz(65) in rims. Amphibole display similar evolution with actinolite replacing tremolite in a fracture pattern recognised in backscatter images. FIA4 Fluid inclusions are only found in epidote cores. Fluid inclusions in the epidote cores correlate with fluid inclusions with the higher antarcticite melting temperatures in calcite, and with higher initial melting temperatures.

7.2 Fluid evolution in relation to cooling and uplift of the Bamble sector

The FIA3 isochors intersects the PT-path of Nijland et al. (1993).at low T and P after uplift (not shown). However, the low T and P intersection does not agree with the observation that FIA3 formed close to the brittle-ductile transition during thrust related deformation. Previous studies of the retrograde assemblages ignore the effect of salts and CO_2 although, as previously demonstrated for the Bamble fluids salt and CO_2 contents do in deed vary considerably. Accordingly, we will here attempt to re-evaluate the P-T evolution taking in to consideration, the fluid evolution.
The peak T conditions are well constrained to 6-7 kb, 700-750°C (Nijland and Maijer, 1993) and corresponds to the stage when the FIA1 fluids (pure CO2), co-existed with partial melts forming the quartz-garnet symplectites.

In order to unravel the poorly constrained retrograde evolution, we designed phase diagrams with the PERPLEX programming package (Connolly, 1990; Connolly, 1995; Connolly, 2005; Connolly and Petrini, 2002) and an updated version of the HP98 thermodynamic dataset (Holland and Powell, 1998) for the PTX_{fluid}-estimations. This combination facilitated the construction of phase diagrams including fluids of variable composition. We implemented our own data in combination with the mineral data and petrographic observations of (Nijland et al., 1993). A common problem, also experienced in the current study, is to simplify the chemical complexity in terms of chemical components, mineral solid solution models, and overlapping phase stability fields. Accordingly, to recognise the correct equilibria is complicated by the fact that phase stabilities of complex systems are determined by high-variance equilibria rather than the more simple univariant equilibria of the conventional petrogenetic grids (Connolly and Petrini, 2002). Commonly this challenge is partially solved by fixing the bulk composition and to calculate ($PT\text{-}X_{fluid}$) pseudosections. Here, the obstacle is to define a so-called thermodynamically effective bulk composition (e.g. Stuwe, 1997). Not least, because the thermodynamic bulk composition may change during cooling as a result of metamorphic differentiation and mineral zonation. The degree of changes in the thermodynamically effective bulk composition during cooling also increases with grain size, because successively larger parts of the grains are removed from the reactive volume of the rock (Stuwe, 1997). Apparently, this scenario is clearly illustrated by the zoned amphiboles described in Sørensen et al. (2007, paper 3) where the strong zoning pattern is maintained as a result of progressively shortening the diffusion distances during exhumation and cooling. However, temporal and spatial variations in fluid availability are also factors controlling the amphibole zonation.

In conclusion, the PT-conditions can not be modelled on the assumption that the retrograde mineral assemblages are products of equilibrium solid-solid net reactions with higher grade minerals as reactants and with the thermodynamic composition comprised by the bulk rock volume. A more reasonable approach is to test the stability of the product phases (retrograde assemblages). For the chemically more complex phases the bulk composition was normally fixed, although, in some cases, this

approach was inhibited by the pronounced mineral zonation. Rather, it is preferred to use the modal proportions of retrograde minerals to estimate a hypothetical bulk composition.

The retrograde reactions include mixed volatile reactions that are difficult to portray in traditional PT phase diagrams because the phase boundaries varies as a function of fluid composition. Traditionally such systems are expressed as P or T-XCO_2 Schreinemakers projections. This method is only applicable to mixed volatile system if one parameter may be independently constrained and it is difficult to trace limiting reactions if this is not the case (Connolly and Trommsdorff, 1991). In an alternative method, the fluid is defined as a solution phase (Connolly and Trommsdorff(1991) in using a pseudocompound approximation (Connolly and Kerrick, 1987) for the fluid to calculate a P-T Schreinemakers projection including a fluid of variable composition. Three types of univariant curves can be traced in such a diagram; (1) true univariant volatile neutral, (2) true univariant volatile dependant, (3) P, T or Xfluid extrema (Table 6).

Table 6: Main reaction types in mixed volatile P-T Schreinemakers projections used to interpret phase boundaries in PT-X_{fluid} phase diagrams.

Reaction type	Description
1: True Univariant volatile neutral	The simplest reactions are reactions that involve C+ 1 phases the same proportion of volatile component on both sides of the reaction. The position of these reactions is fixed in PT-space independently of fluid composition. The stability of the assemblages on either side of the reaction boundary however are truncated by volatile components, limiting the stability in PT-Xfluid space.
2: True univariant volatile dependant	Involves c+1 phases including the fluid of variable composition. The fluid composition varies along the reaction curve i.e. the PT-conditions are fixed as a function of P *or* T. Corresponds to pseudoinvariant points in P or T Xfluid (fixed either P or T) Schreinemakers projections.
3. P, T or Xfluid extrema of reactions involving C-phases.	Minima/maxima in T-Xfluid or P-Xfluid of volatile dependant c-phase reactions. In addition fluid end member positions of reactions can also be plotted (i.e. pure H_2O or CO_2). The position of the reaction curve for intermediate fluid compositions are termed pseoudounivariant curves and will plot between the end member curves and the curves of the minima/maxima as isopleths of fixed fluid composition in PT-diagrams..

The calcsilicate assemblages observed in the current study involve equilibria that depend not only on P and T but also on fluid availability and composition. An early retrograde replacements was replacement of the diopside-phlogopite assemblage (Mp1) by tremolite-sanidine-rutile assemblage (Mp2a), tremolite, calcite quartz (Mp2b) and biotite-amphibole (Mp2c). Field and microscopic observations imply that these assemblages formed simultaneously as a function of chemical (i.e. protholith) variations. Mp2a formed in reaction of the Mp1 assemblage with the quartz-biotite-plagioclase gneiss providing excess SiO_2 and K_2O. Mp2b is replacement of diopside. Mp2c formation is more complex as it involves interaction with the chemically complex amphibolite adding Fe to the Fe-Mg phases hence effect solid solutions. Mp2a and Mp2b on the contrary involve only almost pure phases and are more easily

interpreted in PT-Xfluid space. The chemical system comprising Mp1, Mp2a and Mp2b is K_2O-MgO-CaO-Al_2O_3-SiO_2-TiO_2-COH (KMCAS-Ti-COH). Two observations were used to simplify the system: 1. the only carbonic fluid encountered is CO_2, limiting the fluid to the binary H_2O-CO_2 COH-subsystem 2. K_2O and Al_2O_3 are linked in the observed phases and can be joined in one chemical component similar to sanidine/microcline: $KAlSi_3O_8$. As a result, the muscovite bearing equilibria, for example, is not shown. The simplified chemical system comprises $KAlSi_3O_8$-MgO-CaO-SiO_2-TiO_2-H_2O-CO_2. We used the method of Connolly and Trommsdorff (1991) to model the fluid as a binary H_2O-CO_2 fluid. All other phases were considered as pure end members, because Fe-Mg substitution was limited. A simplified version of the results is illustrated in Figure 18, and relevant reactions are summarised in Table 7.

The upper P stability of tremolite + sanidine is limited by the fluid independent univariant reaction 1 toward the assemblage phlogopite + diopside + quartz (Table 7). In addition the assemblage tremolite +sanidine+ calcite is limited by equilibria 2 with a thermal maximum at XCO_2=0.75 and its minimum stability at XCO_2=0 (Figure 18). This is approximately equal to the maximum stability limits of the assemblage tremolite +quartz + calcite (equilibria 3) also at XCO_2=0.75 (Figure 18). Therefore, it is implied that Mp2a and Mp2b formed simultaneously at the same XCO_2-PT conditions. Local presence of calcite in Mp2a is controlled by excess Ca where SiO_2 is scarce. Given that Mp2a and Mp2b formed simultaneously, the assemblages must have formed at the pseudoinvariant point comprising the intersection between reaction 1 and reaction 3 (Table 7, Figure 18). The maximum T conditions corresponds to the intersection of the thermal extremity of reaction 3 with reaction 1 at T=636°C, 7070 bar, XCO_2=0.75. The observation of sanidine gives a minimum T, P of 456°C and 8417 bar (reaction 1).

Reaction 7 defines the stability of the rutile together with sanidine and tremolite. The position of reaction 7 in P-T space depends on XCO_2 in that the sanidine + rutile + tremolite assemblage is stabilised at higher P constant T by increasing XCO_2 (Figure 18). However, at high XCO_2, reaction 7 is pinched against equilibria 8 (Table 7, Figure 18)

Reaction 8 occurs at a higher temperature than reaction 2 and 3 along the reaction 1 curve. Thus the rutile + sanidine + tremolite assemblage is not entirely compatible with the Mp2a and Mp2b assemblages. The stability field is however close at XCO_2=0.75.
The edenite + tschermakite substitution was active in the amphiboles (Sørensen, Austrheim & Larsen, Paper 3, and this paper!). Therefore, amphibole bearing assemblages are stable at higher temperatures hence explain the unexpected stability of rutile. The exact effect of this is difficult to quantify as the observed edenite and tschermakite substitutions vary within the amphiboles in the assemblages. We infer this to be the result of local chemical variations i.e. the Na-content of the rock will control the amount of Al in amphibole at a given temperature. The effects of amphibole solid solutions can only be explored in fixed bulk composition pseudosections. We believe that the corrections made by such pseudosections will only have an illustrative function because the amphibole stability is sensitive to the

thermodynamically effective bulk composition. In conclusion the first retrogression occurred near the maximum thermal stability of the tremolite + quartz + calcite assemblage with a significant CO_2 fraction in the coexisting fluid.

Fluid inclusion studies documents salts in all the retrograde fluids. Salt is decreasing the a_{H2O} and, therefore, an estimated XCO_2 at 0.75 for the onset of retrogression is too high. With a total salinity of 30 wt% NaCl, the true XCO_2 value would only be about 0.23 (Figure 19). Because this is the salinity in the total fluid and we measured 30wt% NaCl equivalent in the aqueous phase both CO_2 and the salinity must be adjusted. Because of the construction of the H_2O-CO_2-NaCl EOS in PERPLEX wt% NaCl is expressed as total wt% in the fluid i.e. wt% NaCl = Xsalt = $wt_{NaCl}/(wt_{NaCl}+wt_{CO2}+wt_{H2O})$, $y(CO_2)^* = nCO_2/(nH_2O+nCO_2)$. In our fluid inclusion studies we indicate the wt% of NaCl in the aqueous phase i.e. wt% NaCl = Ysalt = $wt_{NaCl}/(wt_{NaCl}+Wt_{H2O})$. The two methods of calculating salinity are related through mass balance considerations. The problem is that the fluid composition is determined by the position of the pseudoinvariant point Mp2 as a function of X and that the relation between Xsalt and Ysalt depends on YCO_2*. This was solved by calculating several T-YCO_2* sections, such as the one in Figure 19, at different Xsalt values. Subsequently, the Xsalt and YCO2* of the pseudoinvariant point were plotted on a diagram. Calculated values of Xsalt as a function of YCO2* at fixed Ysalt= 30 wt% were plotted on the same diagram. The intersection between the curve defined by the pseudoinvariant points and the curve of Xsalt at Ysalt = 30 wt% defined the fluid composition at $XCO_2 = (n_{CO2}/(n_{CO2}+n_{H2O}) = 0.32$, $XH_2O = 0.68$, $wt\%NaCl = wt_{NaCl}/(wt_{H2O}+wt_{NaCl})=30wt\%$. In mole fractions of the total fluid this corresponds to $XCO_2 = 0.30$, $XH_2O = 0.62$ and XNaCl=0.08.

The phase diagram in Figure 18 is both showing the probable path of initial retrogression and subsequent retrogression history toward lower T. The assemblage tremolite + sanidine is limited by both the univariant equilibria 1 and the pseoudounivariant equilibria 4. Equilibria 4 is stabilised over sanidine + tremolite by high XCO_2 i.e. is pushed towards higher T. The XCO_2 isopleths of equilibria 4 are closely spaced at high XCO_2. Replacement of sanidine + tremolite by quartz + calcite + phlogopite was not observed. Accordingly, either the XCO_2 decreased rapidly as the temperatures fell or the PT path followed the slope of the equilibria 4 isopleths. The fluid inclusions data strongly support that a rapid fall in XCO_2 is the best approximation.

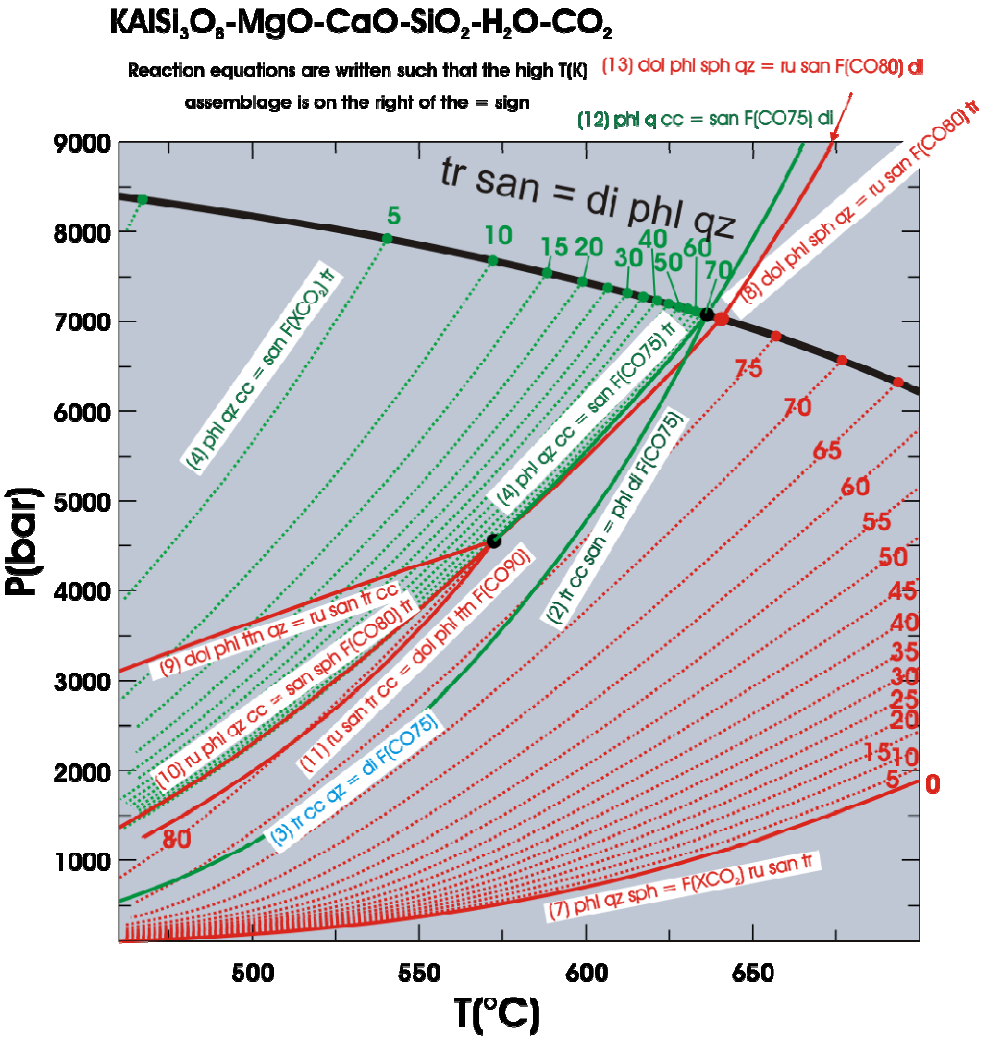

Figure 18: Relevant phase equilibria for Mp1, and Mp2. PT-XCO_2 conditions for the formation of the Mp2 assemblages are defined by univariant, singular (extrema) and pseoudounivariant mineral reactions. Stability of assemblages tr+san and ru+tr+san is partly limited by pseudoinvariant equilibria, which are only univariant PT-curves for fixed fluid composition. Reaction equations do not include stoichiometry. Full reaction equations are found in Table 7. Calculated with PERPLEX (Connolly, 1990) and an updated version of HP98 thermodynamic dataset (Holland and Powell, 1998). The true univariant reaction governing the overall stability of Mp1 over Mp2a is given a thick black line, red lines are reactions involving rutile bearing assemblages, green tr + san ±cc, and blue is the maximum thermal stability limit of Mp2b.

Table 7: Relevant reactions in the $KAlSi_3O_8$-MgO-CaO-SiO_2-TiO_2-H_2O-CO_2 system. The reaction type refers to the terminology in Table 6. Note that muscovite bearing equilibria are not considered in this system. Reactions are written such that the high temperature assemblage is on the right of the ↔ sign.

1	Type 1	tr +san ↔2di+phl+4qz
2	Type 3	2tr+san+3cc ↔ phl+7di+H_2O+3CO_2
3	Type 3	tr+3cc+2qz ↔ 5di+H_2O+3CO_2
4	Type 3	12qz+3cc+2.5phl↔2.5san+1.5tr+3CO_2+H_2O
5	Type 3	tr+3cc↔dol+4di+H_2O+CO_2
6	Type 3	5dol+8qz+H_2O↔3cc+tr+7CO_2
7	Type 3	5phl+6sph+18qz↔2H_2O+3ru+3tr+5san
8	Type 2	(10/4-9/4X)phl+(3-3X)ttn+(9-7X)qz+1/2Xdol ↔ XCO_2+(1-X)H_2O+(3-3X)ru+(6/4-5/4X)tr+(10/4-9/4X)san
9	Type1	2dol+phl+4ttn+4qz↔4ru+san+tr+4cc
10	Type2	ru+phl+qz+Xcc↔san+ttn+tr+XCO_2+(1-X)H_2O, Full reaction equation is with fluid dependent stoichiometry: (4X-3)ru+(2.5-2.5X)phl+(9-8X)qz+Xcc↔ (2.5-2.5X)san+(4X-3)ttn+(1.5-1.5X)tr+XCO_2+(1-X)H_2O,
11	Type2	ru+san+tr+cc↔dol+phl+ttn+(1-X)H_2O+XCO_2 Full reaction equation is with fluid dependent stoichiometry: (6-4X)ru+(1/2X-1/4)san+(3/4-1/2X)tr+(9-7X)cc ↔(9/2-4X)dol+(1/2X-1/4)phl+(6-4X)ttn+(1-X)H_2O+XCO_2
12	Type 3	6qz+3cc+phl=3di+san+3CO_2+H_2O
13	Type 2	phl+ttn+qz+dol=ru+san+di+XCO_2+(1-X)H_2O

None of the assemblages in Mp3, Mp4 or Mp5 are limited by true univariant equilibria and progressive fluid aided metasomatosis during the addition of Na, further complicates the interpretation. However, PT-X_{fluid} extrema along with pseoudounivariant volatile dependant reactions allow for a tentative interpretation. Mp3 comprise the diopside + tremolite+ calcite assemblage whereas Quartz is absent. Therefore, Mp3 was stable above equilibria 3 but below equilibria 2 and 5 (Table 7). Quartz is not in excess because the tremolite diopside assemblage otherwise would have decomposed by equilibria 3. The stability field of the Mp3 assemblage in the K_2O-Al_2O_3-MgO-CaO-SiO_2-TiO_2-H_2O-CO_2 system at 7 kbar is shown in Figure 19. The stability of the Mp3 is narrow in this system. However, the presence of Na, Al and Fe in amphibole would increase the stability hence the shown stability field is smaller than reality. Because XCO_2 is decreasing during retrogression, it is implied that the Mp3 assemblage is locally stabilised by decreasing the XCO_2. Figure 19 also illustrates that the isobaric cooling path is only realised if XCO_2 continuously decreased during cooling. The phase diagram (Figure 19) also imply that the diopside bearing

assemblages may only survive retrogression at silica undersaturated conditions hence explaining why the diopside bearing Mp1 assemblage commonly is preserved in a protective shell of Mp2a.

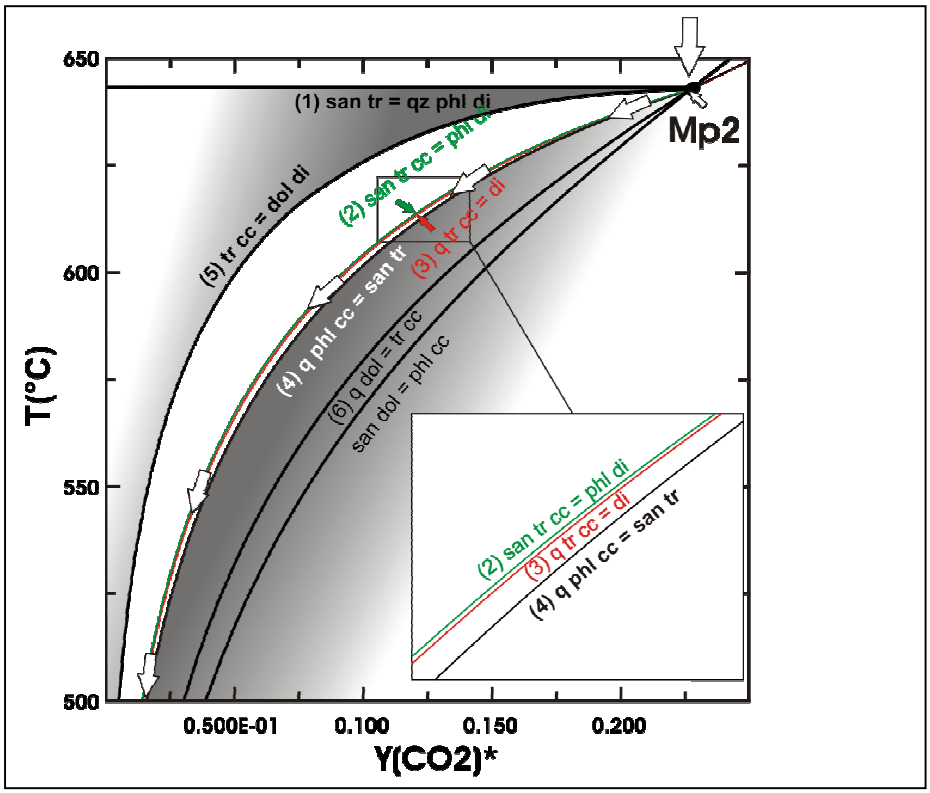

Figure 19: Isobaric T-XCO_2 section at $P=P_{fluid}$=7000 bar for the K_2O-Al_2O_3-MgO-CaO-SiO_2-TiO_2-H_2O-CO_2-NaCl system showing the stability field of Mp3 between the red and green reaction curves. White arrows illustrate possible fluid evolution during cooling. The grey shading show the limits of the T-fluid space constrained by reactions quartz+dolomite+phlogopite and tr+cc = dol +di. It should be kept in mind that the section is only illustrative and that the narrow stability field of Mp3 is probably larger because of solid solution in amphibole. Mp3 stability can only be constrained if one thermodynamic parameter may be independently fixed. In addition the diagram uses Mg-endmembers and does not take into account the edenite and tschermakite substitution in amphibole. Reaction equations are written such that the high temperature assemblage is to the right of the = sign. Calculated with PERPLEX and an updated version of the HP98 dataset. $YCO_2^*=n_{CO2}/(n_{H2O}+n_{CO2})$.

Amphiboles of the Mp4 assemblage are more Al, K and Na rich than other amphiboles in the calcsilicates. Therefore, both edenite and tschermakite substitution was important in the Mp4 amphiboles and Na was an important component that

stabilised the Mp4 assemblage. The Mp4 assemblage could not form from the Mp1 assemblage, without adding Na to the bulk composition. Given the flexibility of the amphiboles in P-T-X space they can not be used to constrain PT-X_{fluid} conditions in this case.

The stability of the Mp5 assemblage (epidote-calcite-tremolite/actinolite-pyrite assemblage related to FIA4) is probably a greenshist-subgreenshist facies assemblage. The stability of this assemblage depends on activity-activity relations in the coexisting fluid phase (Bird and Spieler, 2004). Core to rim increase in the Fe-content of both epidote and amphibole could be an effect of both PT-changes and small variations in fluid composition. Figure 20 outline the effects of variations of cation to hydrogen ratios in the coexisting fluid on phase equilibria in the CaO-Al_2O_3-Fe_2O_3-SiO_2-H_2O-HCl system at fixed P and T. From this it appears that compositional changes of epidote may be controlled by the fluid composition. For example, calcite dissolution change the cation speciation and increase pH hence increasing the Fe-content of epidote from Xps = 0.15 to 0.27 (Bird and Spieler, 2004). However, the decreasing $CaCl_2$ content in the fluid inclusions associated with the increased pistacite content in epidote, contradicts this explanation. Rather, the increasing pistacite is due to increased Fe^{3+}/Ca ratio of the fluid. This interpretation is supported by the lowering of the first melting temperatures observed parallel with the increased Fe content in the epidote grains. Accordingly, lowering of the first melting is enhanced by increasing the complexity of the fluid system. However, Figure 20 is only a principal sketch and is only partially explaining the evolution.

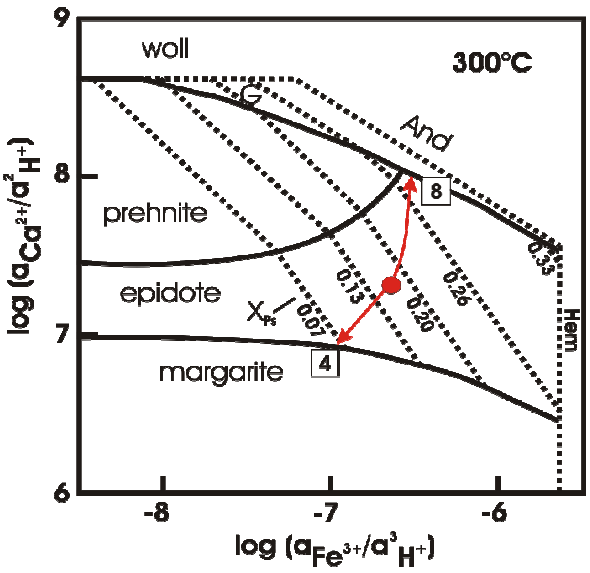

Figure 20: Activity-Activity diagram showing the phase relations in the system CaO-Al_2O_3-Fe_2O_3-SiO_2-H_2O-HCl as a function of cation to hydrogen ion activity at P=86 bar in the presence of quartz and fluid with unit activity of water. Stability fields of phases in the system are shown by solid lines. Prehnite, epidote and garnet (G) all involve solid solution between Fe3+ and Al. Stippled lines show isopleths of constant Fe-content with labels denoting the equivalent Xps content in the epidote field. Arrows represent changes in epidote predicted by theoretical irreversible reaction path models of anorthite and calcite reactions with aqueous solution, labelled 4 and 8 respectively in the diagram. From Bird and Spieler (2004). More information on sources of thermodynamic data is

found therein. The diagram is purely illustrative in our case but demonstrates the high variance of epidote bearing assemblages, which are sensitive to small changes in fluid composition.

Nijland et al. (1993) provide excellent field and petrographic documentation of the paragenetic evolution during cooling and uplift observed in corundum bearing rocks from Kleggåsen in near vicinity of our study area. Their study includes parageneses formed during retrogression of a rock originally comprising corundum + plagioclase + biotite +rutile + sillimanite(MI). Nijland et al.(1993) define three main retrograde stages:

MII: Kyanite-muscovite chlorite veins intersecting MI

MIII: Assemblage corundum + margarite replacing kyanite in MII and corundum + plagioclase in MI.

MIV+MV: a mixture of late alterations.

In the following study we provide a detailed revaluation of their interpretation, based on phase diagram calculations.

Nijland et al. (1993) interpreted the formation of the MII veins to be the result of a fluid interacting with the host rock according to the following reaction:

reaction I: The formation of Ky-Ms-Chl veins

$$MII: 3Sil + Bi + 0.5Pl + 4H_2O \leftrightarrow Ms + 0.5Chl + Ky + (0.1Ti, 0.08Mg, 0.2Ca + 0.1Na)$$

The reaction is slightly metasomatic because the composition of the products and reactants deviate. Nijland et al.(1993) used the presence of Kyanite over Sillimanite in conjunction with the textural observation that margaritisation occurred at a later stage, to infer that the reaction occurred at PT 7 kb and 600-700°C,respectively. However, we argue that the reaction must occur in the kyanite field at lower T because chlorite and not biotite was the stable Fe-Mg phase. We used three solution models for the solids: Muscovite model Mica(CH2) (Coggon and Holland, 2002), Chlorite model Chl(HP) (Holland et al., 1998) and biotite model Bio(HP)(Powell and Holland, 1999) and calculated pseudosections for variable XCO_2. The salinity of H_2O is kept constant at 30wt% using an internal fluid EOS in PERPLEX which is calibrated with devolatisation/decarbonation reactions (Aranovich et al., 2005). Nijland pers comm. confirms that he observed brines in MII kyanite as fluid inclusions containing halite; however, he did not study the inclusions in details. The bulk composition was estimated using the stoichiometry of the kyanite forming reaction (reaction I).and the average mineral compositions (Nijland et al., 1993). The resulting pseudosection is shown in Figure 21a. The stability range of the MII assemblage is well constrained in temperature but not in pressure and also depends on the fluid composition (Figure 21a). The stability limits shifts to lower temperatures and pressures with increasing XCO_2(Figure 21a). According to Nijland et al. (1993) the low temperature limit of the MII is defined by the stability of corundum and plagioclase over margarite i.e. the

onset of margaritisation. However, as documented below, this assumption is contradicted by the fact that MIII and MII have overlapping stability fields. Note that the MII stability field is not univariant but has a variance of 5, meaning that 4 thermodynamic parameters must be fixed to constrain the MII field.

The MIII comprise margarite + corundum (Nijland et al.(1993) and formed from metasomatic replacement of kyanite. This replacement reaction must involve a Ca^{2+} + Na^{+} bearing fluid. A number of reactions were suggested for this replacement. In common, they all involve cation exchange with a fluid phase (see Nijland, (1993) for references). Stabilisation of the margarite + corundum requires the decomposition of quartz and removal of SiO_2 (Nijland et al.(1993) by for example reaction II):

reaction II: reaction suggested by Nijland et al. to be responsible of the metasomatic replacement of kyanite (ky) by margarite Marg plus corundum:

$$3\mathrm{ky} + \mathrm{Ca}_{(aq)} + 3\,\mathrm{H_2O} + 0.5\,\mathrm{O_2} = \mathrm{Mrg} + \mathrm{Cor} + \mathrm{Si(OH)_4}$$

Bucher et al.(2005) use thermodynamic modelling to demonstrate that removal of SiO_2 generates excess Al_2O_3. SiO_2 is removed in a chemical gradient by lowering the chemical potential of SiO_2 in the forsterite + talc assemblage in the surrounding ultramafic rocks.

In Froland, this is not applicable because the corundum-bearing rocks are surrounded by granitic gneisses with excess SiO_2.

Accordingly, kyanite decomposition must be re-evaluated. It is suggested that the following reaction was responsible for the replacement of kyanite by margarite + corundum:

reaction III:our model for metasomatic replacement of kyanite by margarite-paragonite solid solution (MaPa) and corundum (cor). Note that reaction stoichiometry depends on margarite composition and that for pure endmember margarite no corundum would form as the result of kyanite breakdown:

$$(3 - \mathrm{X})\mathrm{ky} + \mathrm{XNa}_{(aq)} + \mathrm{XCa}_{(aq)} + \mathrm{H_2O} + (0.25 + 0.25\mathrm{X})\mathrm{O_2} =$$
$$(1.5 - 1.5\mathrm{X})\,\mathrm{Cor} + \mathrm{MaPa}(\mathrm{Xma}, (1 - \mathrm{X})\mathrm{pa})$$

Accordingly, the margarite + corundum formation is a function of cation activities in the fluid phase as well as of P and T. As a result the margarite forming reaction is difficult to portray in PT-diagrams.

To characterise the P-T-X properties of the margarite + corundum assemblage it is easier to assume solid-solid reactions. This approach requires the hypothetical modelling of the assemblages that would have formed instead of corundum + margarite given different PT-conditions for the same bulk composition (reaction III). Given that only one silicate-reactant is present (ky) (1 mole p.f.u.) and Al_2O_3 (1 mole p.f.u.) the bulk Al/Si ratio is locked at 1. In addition the Ca/Na ratio is fixed by the margarite composition, which again fixes the Si content and hence the Al content of the products.

Using these constraints on the bulk composition we calculated pseudosections to test the stability of the margarite + corundum assemblage. The first step is to calculate isobaric T-XCO_2 pseudo sections to constrain the fluid composition. As above, the salinity is fixed at 30 wt% using the same fluid EOS as for MII and solution models Pl(h) (Newton et al., 1980) for plagioclase and Mica(CH2) for margarite. The results document that the stability field of the MIII assemblage is considerably larger than that reported by Nijland et al (1993) (Figure 21b). The upper limit is quite similar, but the lower limit is expanded. Similar results were found by constructing pseudosections for the replacement of the MI assemblage by margarite + corundum. Because the results are similar only one diagram is present here. The difference in the lower T limit of MIII between our estimate and the Nijland et al. (1993) is caused by the fact that Nijland et al. (1993) defines the lower limit of MIII by the absence of zoisite/clinozoisite and the reaction:

reaction IV: Low temperature ilmit of MIII according to Nijland et al. (1993)

$$5An + 2H_2O \leftrightarrow Mrg + 2Zo + 2SiO_2$$

However, there are two observations that rule out reaction IV. First, the reaction will, as also noted by Nijland et al. (1993), shift to lower T with increasing Xab in plagioclase. Second, and most important, the stability of zoisite in the CNASHC system depends on the bulk composition and/or cation composition of the coexisting fluid (Rosing et al., 1987). In conclusion, the reaction suggested by Nijland et al. (1993) is contradicted by the bulk composition which prohibits the stabilisation of zoisite/clinoziosite, which would need higher Ca-content of the system. Most importantly, the PT-stabilities of MII and MIII are coinciding (Figure 21). Therefore, the paragenetic change from MII to MIII is not related to PT changes.

Studies of the hydration of corundum + plagioclase imply that the fluid cation composition controls the hydrated assemblages (Rosing et al.(1987). Activity diagrams show that the stability of margarite + corundum at 550°C and 5 Kb is possible in fluids with a SiO_2 activity of about 0.1, log (aCa^{2+}/a^2H^+) of about 6 and low log (aK^+/aH^+) (Rosing et al.(1987). Increased K^+ contents of the fluid relative to H^+ and Ca^{2+}, stabilise muscovite over margarite. Therefore, the change from MII to MIII probably reflects increased Ca^{2+} relative to K^+ in the fluid phase. This scenario agrees with the fluid inclusion observations that record changes in the cation composition from the NaCl-KCl-H_2O-CO_2 (FIA2) to NaCl-$CaCl_2$–H_2O (FIA3) fluids. In conclusion, the shift from MII to MIII marks the transition from potassic to sodic alteration and is constrained to the MIII stability field in the Froland area, at about 550 to 450 °C, and P > 4500 bar.

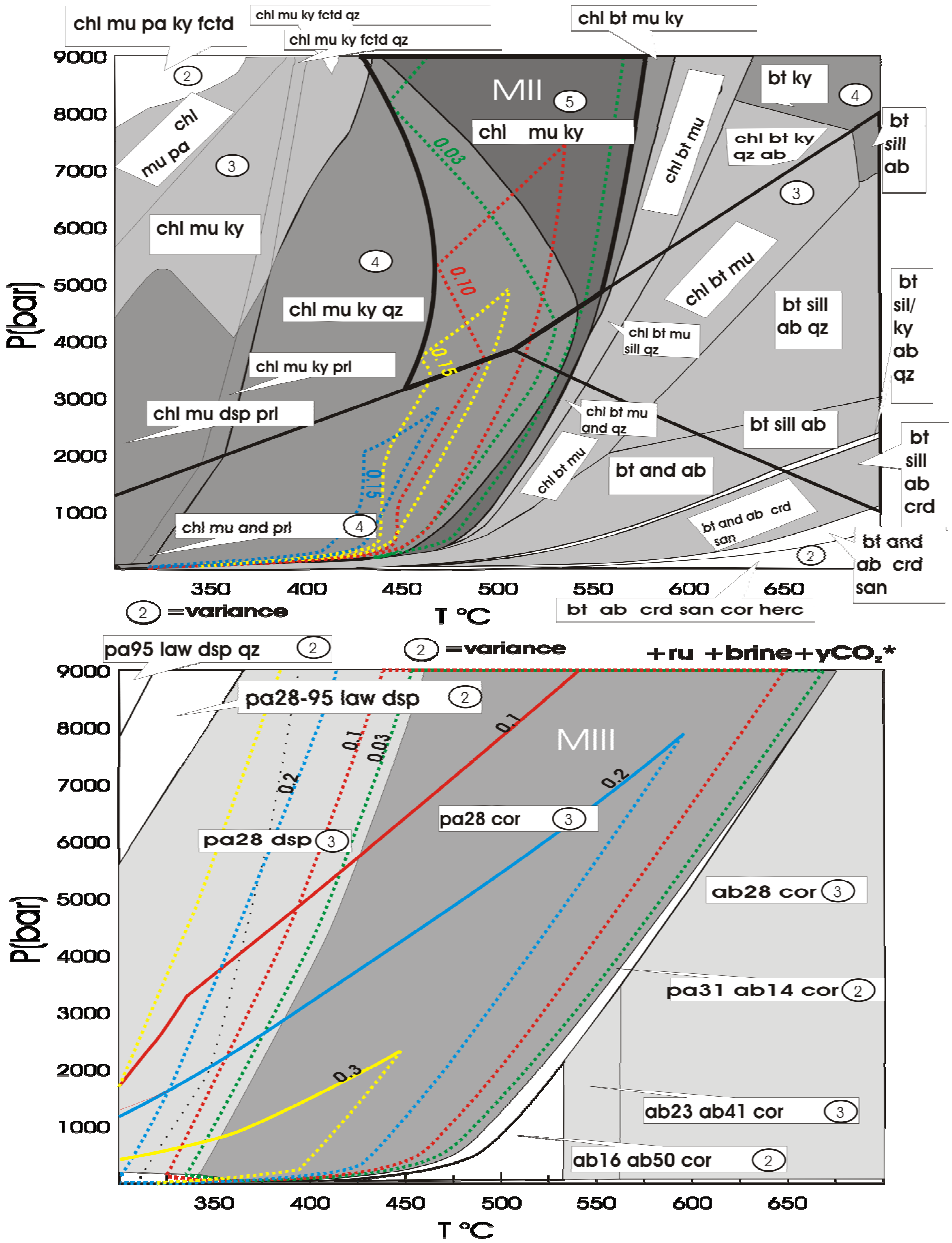

Figure 21: Pseudosections representing metamorphic stages MII and MIII of Nijland et al. (1993). A) MII comprising the assemblage Kyanite (Ky)-Chlorite (Chl)-and muscovite (Mica(CH2)). The stability field is dependant on fluid composition and shifts to lower

pressure with increasing XCO_2 in the coexisting fluid (coloured lines). The pressure is broadly constrained by the stability of kyanite. B) MIII comprising Margarite and corundum has a larger stability field than MII. Isopleths show change in the stability fields for various XCO_2 values. Both assemblages are less stable in CO_2-rich than in H_2O rich fluids. The stability fields of MII and MIII overlap but the MIII assemblage has a larger stability field and would have stabilised before MII if only P and T were changed at constant fluid compositons. Pseudosections were calculated with PERPLEX (Connolly, 1990; Connolly and Petrini, 2002) and an updated version of the HP98 dataset (Holland and Powell, 1998).

7.3 Tentative PT-fluid path

The aim of this section is to propose a tentative PT-for the Froland area (Figure 22).

The first retrograde assemblage that may be used for the P-T path is the tremolite + sanidine assemblage (Mp2a). The stability of the Mp2a assemblage is limited by the univariant reaction diopside + phlogopite + quartz (Figure 22). As previously discussed the Mp2a and Mp2b assemblages probably formed simultaneously hence the PT-condition lie on a pseudoinvariant point. This interpretation is supported by the assemblage tremolite + calcite + sanidine in Mp2a, which has similar stability field as Mp2b (Figure 22). The stability of rutile + sanidine + tremolite/actinolite within Mp2a is not compatible with the model system, where the Fe, Al, Na and K content of amphibole was not considered. However the stability of the rutile bearing assemblage increases at high XCO_2 in the fluid. Thus we make the semi-quantitative interpretation that XCO_2 in the fluid was high when Mp2a and Mp2b formed and that they formed near their maximum thermal stability in the model system.

Mp2c, comprising amphibole + biotite, forms from the Mp1 diopside + phlogopite assemblage toward amphibolite. Field observations suggest that Mp2c is related to the biotite-amphibole assemblages in the amphibolite. Thus the semi-quantitative estimate provided by the calcsilicate assemblages Mp2a and Mp2b probably serves as an estimate of the initial PT-X fluid conditions for the first introduction of biotite in the amphibolites and the quartz type named Qz2. Qz2 in quartzites coexists with rutile hence the Ti in quartz geothermometer of Wark and Watson (2006) is applicable giving a temperature of 626°C. This agrees well with the paragenetic data of the calcsilicates and suggests that Qz2, introduction of biotite in amphibolites, and formation of the tremolite + sanidine assemblage were all related to the same early retrograde stage (Figure 22). The fluid inclusions in FIA2 comprise brine fluids. The presence of brines in the fluid would serve to reduce the activity of H_2O and hence the XCO_2 predicted by the model system with binary H_2O-CO_2 fluid. In conclusion we infer that Mp2 formed at c. 626-640°C and 7000 bar with a fluid with about 30 wt% salts and $XCO_2 = (n_{CO2}/(n_{CO2}+n_{H2O}) = 0.32$.(Figure 19).

The tremolite-sanidine assemblage (Mp2a) is well preserved suggesting that the assemblage phlogopite + calcite + quartz was not introduced during cooling by

reaction 4 (Table 7). Isopleths of reaction 4 are closely spaced (Figure 18 and Figure 19) suggesting either that the PT-path followed the isopleths or that the fluid composition changed towards much more H_2O rich compositions during early cooling.

Later mineral pargenises in the calcsilicates are constrained by high variance equilibria that depend on both the fluid composition and the chemical complexity sustained by increasing the amount of Al and Na in amphibole and by increasing the Fe content in amphibole.

The next stage in the fluid and PT evolution is better characterised by Nijland et al.(1993). MII and MIII are interpreted to comprise two sepapare PT-events (Nijland et al. 1993), however, they probably formed at similar PT-conditions, but at different cation composition of the coexisting fluid. MII is characterised by activity-activity diagrams in Rosing et al.(1987). MII formed with a KCl bearing fluid, whereas MIII formed with a $CaCl_2$ bearing fluid. This transition is preserved in the FIA2 to FIA3 transition and marks a change from potassic/sodic to sodic/calcic alteration. This event occurred at 425-575 °C, minimum pressure of 4500 bar given the stability of kyanite.

The only data that are available for the uplift path is the isochore of FIA 3, which formed during exhumation near the brittle-ductile transition of quartz. In addition the lack of decrepitation textures in relation to FIA3 suggests that the pressure difference between the uplift path and the FIA3 isochore was smaller than the decrepitation strength of fluid inclusions in quartz. Bodnar et al.(1989) determined an empirical relation between inclusion size and decrepitation strength in quartz:

$P(kbar)=4.26\ D^{-0.423}$ where D is the inclusion diameter in microns

With an inclusion size ranging from 5 to 10 microns this gives strength between 1608 and 2156 bar.

The last part of the retrograde path is constrained by coexisting prehnite and pumpellyite and fluid inclusions at 175-280 °C and 2-3 kb (Nijland et al., 1993; Touret, 1985). We infer an uplift path through the isochore of FIA3 down to this point, between 300-400°C, from 5-7kb and down to 2-3 kb. Isopleths of the reaction calcite + rutile +quartz $\leftrightarrow$ titanite indicates that XCO_2 was lower than 0.001. This strengthens the validity of our inferred PT-X fluid uplift path. Our inferred PT-path is presented in Figure 22. It is pushed towards considerably lower temperature than the PT path of Nijland et al. (1993) in agreement with our fluid inclusion data. The PT-path suggested here imply fast uplift at a low temperature. This agrees with the partly brittle partly plastic behaviour of the Bamble rock during uplift.

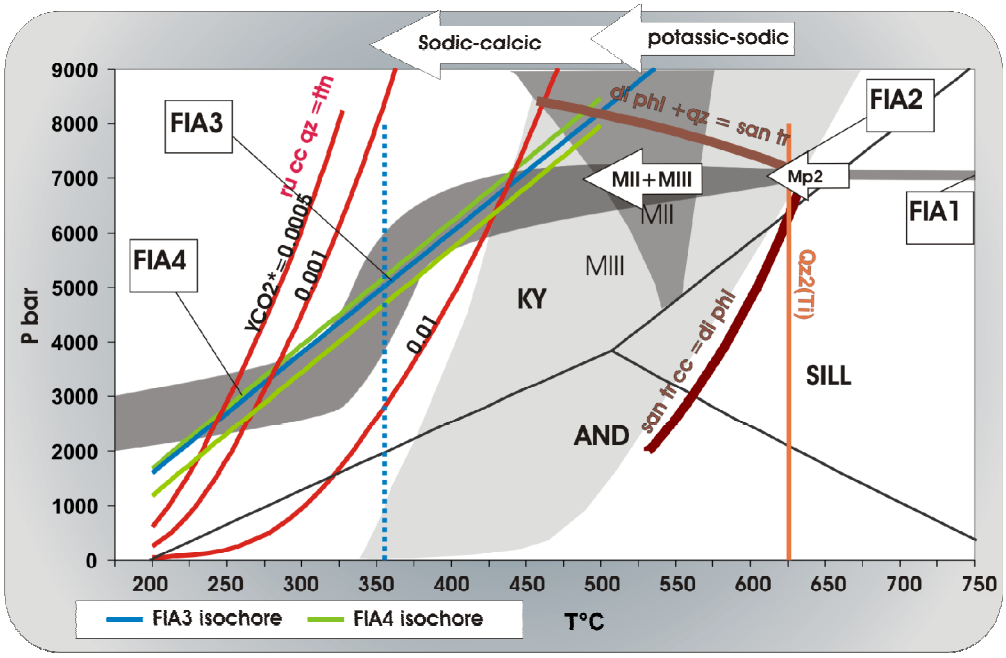

Figure 22: Tentative PT-Xfluid path of the study area, with possible implication for the uplift path of the Bamble sector. The PT-X_{fluid} path is assembled using a combination of mineral paragenetic and fluid inclusions data. Because fluid inclusions and mineral paragenesis that are simple enough to be portrayed quantitatively in PT-space the correctness of the PT-path rely on textural correlations between assemblages in one rock type and fluid inclusions found in other rock types. Arrows on the top of the diagram indicate condition when alteration changed from potassic

7.4 Quartz recrystallisation and purification, the role of the fluid

High purity quartz, the Qz3 of Sørensen and Larsen (2007), formed when the fluids were dominated by NaCl with minor $CaCl_2$. These fluids form quartz with mm-scale recrystallisation textures in a channel like pattern, not only lowering the luminescence of the quartz but also removing most impurities including the rutile needles.

The solubility of quartz in pure water displays a general increase with P and T. However, the solubility is also a function of the fluid composition. Except for an initial salting in effect at low salinity and pressure, the presence of salts has a negative effect on the quartz solubility. Similarly the presence of non-polar dissolved species like CO_2 will have a stronger effect (e.g. Newton and Manning, 2000; Shmulovich et al., 2006).

Aqueous brines have lower wetting angles against quartz than low salinity fluids (e.g. Watson and Brenan, 1987). This enables brines to infiltrate quartz on a fine scale

via micro-pores. CO_2 or other non-polar dissolved species will have the opposite effect (Watson and Brenan, 1987). The increased infiltration capability of brines counteracts the effect of the lower solubility of quartz in brine, because the high degree of infiltration increases the surface area of quartz which is exposed to the fluid. We also suspect that the quartz recrystallisation observed is not simply a process of dissolution and re-precipitation, but also a process of minimising the free energy of quartz at the given PT-X_{fluid} condition, i.e. quartz with specific trace element configurations will be stable. However it is inferred from our study that a fluid phase is needed for reaction to occur.

The type of recrystallisation depends also on the PT path and the gradients in the quartz solubility. If the solubility is increased along the PT-path then narrow dissolution textures will be dominant. On the contrary, if the solubility decrease along the PT-path, it is more likely that the dissolved quartz will be redistributed locally.

Therefore, we believe variation in quartz solubility gradients is the background for the difference between the Qz3 and Qz4 textures i.e. Qz3 formed in a PT-envelope where the quartz solubility decreases with temperature, whereas Qz4 formed with increasing quartz solubility with temperature. $CaCl_2$ in fluids decrease the quartz solubility more than NaCl (Shmulovich et al., 2006), suggesting the change in fluid cation speciation from Na dominated to Ca dominated also served to decrease the quartz solubility. Furthermore, the presence of carbonates in fluid inclusions in Qz4 document that CO_2 was present hence reducing the infiltrating capability of the fluids.

7.5 The fluid evolution as a result of fluid rock interaction

The retrograde fluids maintain a high salinity throughout the retrograde uplift path. However, the cation speciation is changing. The first retrograde fluids are mixtures of NaCl-KCl-H_2O-CO_2 with eutectic salinity and introduced together with low salinity H_2O-CO_2 mixtures. CO_2 is absent in the subsequent fluids and their cation composition changes. The evolution in cation composition can be described in the H_2O-NaCl-KCl-$CaCl_2$ tetrahedron (Figure 23). The cation composition experience significant changes at constant salinities in going from

NaCl-KCl → NaCl-$CaCl_2$ → $CaCl_2$ (Figure 23). Probably this evolutionary path is the result of fluid rock interactions at variable P and T under the formation of various mineral assemblages (Table 8).

The aqueous phase in FIA2 comprises near eutectic NaCl-KCl-H_2O mixtures. This agrees with the observation that potassium required for biotite formation was introduced to the amphibolites by a fluid phase. Beach (1980) suggested the following reaction for the formation of biotite in retrograde shearzones in amphibolites in the Lewsian complex:

$$2Na_{0.5}Ca_2(Mg, Fe)_{4.5}Al_{0.5}Si_7AlO_{22}(OH)_2 + 2K+ + 16H^+ \leftrightarrow$$
$$K_2(Mg,Fe)_{4.5}AlSi_6Al_2O_{20}(OH)_4 + 8SiO_2 + 4.5(Mg,Fe^{2+}) + 4Ca^{2+} + Na^+ + 8H_2O$$

Which is a reaction consuming K and producing H_2O, Mg, Fe, Ca and Na. In the study area, however, the formation of biotite coincides with the formation of a new amphibole which is chemically different from the old amphibole. The composition of the newly formed amphibole and biotite varies, but the distribution of octahedral cations between biotite and amphibole follows a univariant trends (paper 3, Sørensen et al., 2007). This suggests that biotite and amphibole in the area formed under similar conditions and that the observed compositional variations in both minerals is caused by variations in the temperature (paper 3, Sørensen et al., 2007). An interesting aspect is that the compositions of the overgrowth rims follow the same trend throughout area whereas amphibole cores follow different trends. Sørensen et al.(2007, paper 3) infer this to be the result of a change in the rock/fluid system from being internally buffered to being externally buffered. The implication is that the retrograde fluids throughout the area have an external source that, after a brief period with internal buffering changed from a low salinity H_2O-CO_2 mixture to a H_2O rich brine. This is mirrored by univariant trends of amphiboles and the linear correlations between X_{Fe} in coexisting amphiboles and biotites. These trends imply that the equilibrium between amphibole and biotite is controlled by an externally derived fluid that stabilises progressively more Mg-rich biotite and amphibole due to exhumation and cooling.

Although an external fluid was supplied, the fluid cation speciation continuously equilibrated with the ambient mineral assemblages. The formation of biotite from amphibole leads to a K-loss and Na-gain in the fluid. This was partially balanced by increased albite contents of plagioclase. However the consumption of K by the formation of biotite and by replacement of plagioclase by K-feldspar lead to a loss of K and a gain of Na and Ca in the fluid hence shifting the composition towards the NaCl-$CaCl_2$-H_2O ternary and FIA3 (Figure 23, Table 8). CO_2 is absent in FIA3 and Three factors may influence the loss of CO_2:

1. Stabilisation of carbonates under the consumption of CO_2 from a limited CO_2 reservoir. However, having an open system this is hardly the case
2. The high salinity of the aqueous phase increases the liquid immiscibility of H_2O and CO_2 (e.g. Bowers and Helgeson, 1983). As FIA2 comprise two separate fluid types, one CO_2-rich low salinity fluid and brine with low CO_2, it is likely that the two fluid types were not miscible at the entrapment conditions. As concluded before however it is not possible to determine if the fluid inclusions formed by phase separation or they are the result of partial fluid mixing.
3. Brine fluids migrate more easily in silicate rocks than CO_2 rich fluids because of their lower wetting angles (e.g Watson and Brenan, 1987). Thus brine and CO_2 rich fluids probably differentiate along the transport pathway after phase separation.

Because of the high salinity of the observed salinity of the fluids, CO_2 is not likely to have infiltrated on along the grain boundaries like the brines. Thus CO_2 may have been restricted to wide channels in the shear-zone system and escaped.

The increased Ca/Na ratio that followed FIA3 may relate to the Na consumption of plagioclase consuming and addition of Ca to the fluid.

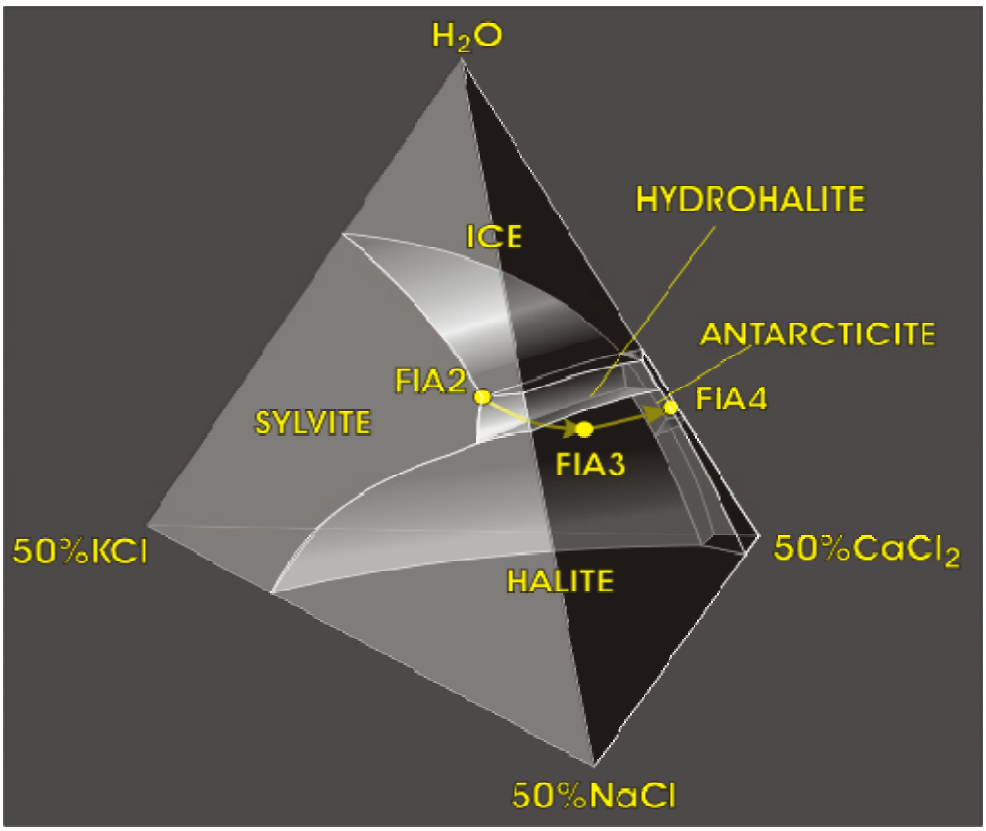

Figure 23: Partly schematic polythermal projection of the H_2O rich part of the H_2O-NaCl-KCl-CaCl2 system after Kornerup-Madsen (1979) showing a three-dimensional impression of the observed cation and salinity evolution of the fluid in relation to the low temperature phase relations observed in microthermometry experiments

Table 8: The fluid evolution interpreted as a result of fluid-rock interaction. See text for discussion.

Occurrence	Type	Petrologic significance
FIA1		
Qz1 Garnet quartz symplectite and partial melting	CO_2 dominated fluid. Internally buffered (closed system)	Variable high grade conditions and partial melting in amphibolite
Influx of aqueous brines mixing with CO_2-rich fluids, open system		
FIA2		
Qz2 in en echelon quartz veins intersecting amphibolite	Juxtaposed 1: H_2O -NaCl-(KCl) - CO_2 H_2O rich eutectic brine 2: H_2O-CO_2 CO_2-rich low salinity fluid	K-metasomatism causing growth of biotite and alteration of amphibole. Around qz-veins equilibrium decussate biotite and amphibole forms, but inside the amphibolite, amphibole grains are only partly altered with rim-core variations
K supplied to rock by fluid and Na exchanged into fluid, from replacement of plagioclase by K-feldspar and formation of biotite from fluid components + amphibole components.		
FIA3		
Qz3 in quartz-scapolite veins in quartz-biotite gneiss	LVS NaCl-$CaCl_2$-H_2O 25wt% NaCl 6wt% $CaCl_2$	Breakdown of rutile and calcite and growth of scapolite from plagioclase, though coupled mineral reactions: ru+cc+qz↔ttn, ru+Ca(aq)+qz↔ttn pl+cc+Na(aq)+Cl(aq)↔scp
Continuous reaction between plagioclase and fluid exchanging Na from fluid into plagioclase and Ca into fluid as plagioclase becomes more albite rich during cooling		
FIA4		
Fluid inclusions in calcite and epidote in tremolite-epidote-calcite apophyllite vug-assemblages	LV inclusions with 31-36 wt% $CaCl_2$ equivalent, the presence of Fe^{3+} suggested by changes in Fe content of epidote and lowering of first melting, Tm_i-ice	Stabilisation of pyrite over pyrrhotite adds Fe to the silicate assemblages in the calcsilicate. This stabilises epidote. As significant amounts of calcite is found and no CO_2 detected in the fluid inclusions implies a large fluid/rock ratio.

7.6 Other studies of the retrograde fluids and alteration assemblages in the Bamble sector

Several studies now document the occurrence of brines in the Bamble sector and their effects on mineral equilibria. Nijland and Touret (2001) documented how a graphic pegmatite was replaced by albite-actinolite-clinopyroxene intergrowths, involving considerable modification of the bulk composition via mobilisation of Al_2O_3 and K_2O and addition of Na_2O. Their fluid salinities are comparable to our study, but they do not report the cation composition of the fluids.

Brine fluids facilitate both mass transport and chemical modification of the rocks they are infiltrating. They also affect volatile bearing metamorphic equilibrium reactions in two ways:

1: The presence of salts reduces the activity of water. This shifts the hydration reactions to a lower temperature compared to the $P = P_{H2O}$ models used in many petrogenetic grids.
2: Hydrous silicates such as amphiboles, biotite and scapolite contain halogens. Several studies imply that halogens in hydrous minerals affect both the SRO (short range order) and LRO (long range order) between elements in the mineral structure. Such effects may be different between different mineral species, and may effect exchange reactions commonly used in geothermobarometry like the garnet biotite exchange thermometer (e.g. Kullerud, 1995).

Nijland et al.(1998) suggested that localised formation of orthopyroxene outside the granulite facies area of the Bamble sector was induced by the local action of brine fluids, which reduced the activity of H_2O, hence shifting dehydration equilibria to lower temperatures.

Alteration assemblages revealing evidence of significant mass transfer are frequently reported from the Bamble sector. Although we only report data from a geographically limited area we hold that brines are the prime suspect of the mass transfer in the Bamble Sector as a whole. Although no other systematic studies of the retrograde fluids exist, several papers report brines with salinities comparable to those reported here. Several studies also document the chemical alteration experienced by the Bamble rocks (Brøgger, 1934; Bugge, 1965; Elliott, 1966; Frodesen, 1968; Jøsang, 1966; Munz et al., 1994; Munz et al., 1995).

Sørensen et al. (2006, paper 3) suggested that the interaction between the brines and hydrous silicates facilitated Fe depletion in the amphibolites and in addition documented direct association between Fe-Cu sulphide formations and alteration of amphibole. Increased understanding of the interaction between hydrous minerals and Cl-bearing fluids, detailed petrographic, geochemical, mineralogical and fluid inclusion studies are needed in order to fully understand the alteration processes in the Bamble sector.

8 Conclusions

1. Brines dominated throughout the cooling and uplift path. CO_2 was quickly expelled during initial stages of retrogression. Salinities in the aqueous phase comprised approximate 30 wt% NaCl equivalents throughout cooling and uplift.
2. A revised retrograde PT-path is suggested based on phase diagram modelling including the effect of the high salinity on retrograde mineral reactions.
3. First introduction of aqueous brines coincides with the brecciation of quartz and dissolution reprecipitation leading to the Qz1 and Qz2 quartz SEM-CL textures and with the first retrograde stage observed in calcsilicates. Ti in quartz thermometry and PT-conditions constrained by phase diagrams agrees on formation conditions at T=626-640°C and P=7000 bar with a fluid with the approximate composition $XCO_2 = (n_{CO2}/(n_{CO2}+n_{H2O}) = 0.32$, $XH_2O = 0.68$, $wt\%NaCl = wt_{NaCl}/(wt_{H2O}+wt_{NaCl})=0.30$ wt%. In mole fractions of the total fluid this corresponds to $XCO_2 = 0.30$, $XH_2O = 0.62$ and XNaCl = 0.08.
4. A second stage of fluid infiltration is characterised by H_2O-rich brines in the greenshist facies. Fluid infiltration during exhumation caused recrystallisation of quartz and formation of high purity quartz (Qz3) and reaction with plagioclase and calcite to form scapolite.
5. Late post kinematic fluids found in vug assemblages are also brines, testifying that a high salinity was maintained throughout the uplift history.
6. The high salinity of the fluid facilitated small and large scale mass transfer in the Bamble Sector.

References

Aranovich, L.Y., Haefner, A., Connolly, J.A.D., Gerya, T.V. and Ulmer, P., 2005. Experimental determination of H_2O and CO_2 activity-composition relations in the H_2O-CO_2-NaCl fluids by reversed dehydration and decarbonation reaction, manuscript, pp. 822-828.

Bakker, R.J., 2003. Package FLUIDS 1. Computer programs for analysis of fluid inclusion data and for modelling bulk fluid properties. Chemical Geology, 194(1-3): 3-23.

Bakker, R.J. and Jansen, J.B., 1990. Preferential water leakage from fluid Inclusions by means of mobile dislocations. Nature, 345(6270): 58-60.

Bakker, R.J. and Jansen, J.B., 1994. A Mechanism for Preferential H_2O Leakage from Fluid Inclusions in Quartz, Based on Tem Observations. Contributions to Mineralogy and Petrology, 116(1-2): 7-20.

Barth, T.F.W. and Dons, J.A., 1960. Precambrian of southern Norway. Norges Geologiske Undersøkelse, 208: 6-67.

Beach, A., 1980. Retrogressive metamorphic processes in shear zones with special reference to the Lewisian Complex. Journal of Structural Geology, 2(1-2): 257-263.

Bird, D.K. and Spieler, A.R., 2004. Epidote in geothermal systems, Epidotes. Reviews in Mineralogy & Geochemistry, pp. 235-300.

Bodnar, R.J., 2003. Interpretation of data from aqueous-electrolyte fluid inclusions. In: I.M. Samson, A. Anderson and L.J. Marshall (Editors), Fluid inclusions: analysis and interpretation. Short course. MAC.

Bodnar, R.J., Binns, P.R. and Hall, D.L., 1989. Synthetic fluid Inclusions. 6. Quantitative-evaluation of the decrepitation behavior of fluid inclusions in quartz at one atmosphere confining pressure. Journal of Metamorphic Geology, 7(2): 229-242.

Bowers, T.S. and Helgeson, H.C., 1983. Calculation of the thermodynamic and geochemical consequences of nonideal mixing in the system H_2O-CO_2-NaCl on phase-relations in geologic systems - Equation of state for H_2O-CO_2-Nacl fluids at high-pressures and temperatures. Geochimica Et Cosmochimica Acta, 47(7): 1247-1275.

Brøgger, W.C., 1934. On several Archean rocks from the south coast of Norway; II, The south Norwegian hyperites and their metamorphism. 1; 1, 421 pp.

Bucher, K., De Capitani, C. and Grapes, R., 2005. The development of a margarite-corundum blackwall by metasomatic alteration of a slice of mica schist in ultramific rock, Kvesjoen, Norwegian Caledonides. Canadian Mineralogist, 43: 129-156.

Bugge, A., 1943. Geological and petrological investigations in the Kongsberg-Bamble formations Norges Geologiske Undersøkelse, 160: 1-150.

Bugge, A., 1945. Löddesöl skarn forekomst. Norsk Geologisk Tidsskrift, 25: 35-47.

Bugge, A., 1965. Iakttagelser fra rektangelbladet Kragerø og den store grunnfjellsbreksje. Norges Geologiske Undersøkelse, 229: 115p.

Bugge, J.A.W., 1940. Geological and petrological investigations of the Arendal district. Norsk Geologisk Tidsskrift, 20: 71-112.

Coggon, R. and Holland, T.J.B., 2002. Mixing properties of phengitic micas and revised garnet-phengite thermobarometers. Journal of Metamorphic Geology, 20(7): 683-696.

Connolly, J.A.D., 1990. Multivariable phase-diagrams - An algorithm based on generalized thermodynamics. American Journal of Science, 290(6): 666-718.

Connolly, J.A.D., 1995. Phase-diagram methods for graphitic rocks and application to the system C-O-H-FeO-TiO_2-SiO_2. Contributions to Mineralogy and Petrology, 119(1): 94-116.

Connolly, J.A.D., 2005. Computation of phase equilibria by linear programming: A tool for geodynamic modeling and its application to subduction zone decarbonation. Earth and Planetary Science Letters, 236(1-2): 524-541.

Connolly, J.A.D. and Kerrick, D.M., 1987. An algorithm and computer-program for calculating composition phase-diagrams. Calphad-computer coupling of phase diagrams and thermochemistry, 11(1): 1-55.

Connolly, J.A.D. and Petrini, K., 2002. An automated strategy for calculation of phase diagram sections and retrieval of rock properties as a function of physical conditions. Journal of Metamorphic Geology, 20(7): 697-708.

Connolly, J.A.D. and Trommsdorff, V., 1991. Petrogenetic grids for metacarbonate rocks - pressure-temperature phase-diagram projection for mixed-volatile systems. Contributions to Mineralogy and Petrology, 108(1-2): 93-105.

Cosca, M.A., Mezger, K. and Essene, E.J., 1998. The Baltica-Laurentia connection Sveconorwegian (Grenvillian) metamorphism, cooling, and unroofing in the Bamble sector, Norway. Journal of Geology, 106: 539-552.

Crawford, M.L., 1981. Phase equilibria in aqueous fluid inclusions. In: L.S. Hollister and M.L. Crawford (Editors), Fluid inclusions: Applications to Petrology. Mineralogiacal Society of Canada Short course Handbook. MAC.

Elliott, R.B., 1966. Association of amphibolite and albitite, Kragero South Norway. Geological Magazine, 103(1): 1-7.

Frodesen, S., 1968. Petrographical and chemical investigations of a precambrian gabbro intrusion, Hiåsen, Bamble area, south Norway. Norsk Geologisk Tidsskrift, 48: 281-306.

Gleeson, S.A., Yardley, B.W.D., Munz, I.A. and Boyce, A.J., 2003. Infiltration of basinal fluids into high-grade basement, South Norway: sources and behaviour of waters and brines. Geofluids, 3(1): 33-48.

Harlov, D.E., 2000. Titaniferous magnetite-ilmenite thermometry and titaniferous magnetite-ilmenite-orthopyroxene-quartz oxygen barometry in granulite facies gneisses, Bamble sector, SE Norway; implications for the role of high-grade CO_2-rich fluids during granulite genesis. Contributions to Mineralogy and Petrology 139: 180-197

Hedenquist, J.W. and Henley, R.W., 1985. The importance of CO2 on freezing point measurements of fluid: evidence from active geothermal systems and implications for epithermal ore deposition. Economic Geology, 80(5): 1379-1406.

Holland, T., Baker, J. and Powell, R., 1998. Mixing properties and activity-composition relationships of chlorites in the system MgO-FeO-Al2O3-SiO2-H2O. European Journal of Mineralogy, 10(3): 395-406.

Holland, T.J.B. and Powell, R., 1998. An internally consistent thermodynamic data set for phases of petrological interest. Journal of Metamorphic Geology, 16(3): 309-343.

Jøsang, O., 1966. Geologiske og petrografiske undersøkelser i Modumfeltet. Norges Geologiske Undersøkelse, 235: 148p.

Knudsen, T.L., 1996. Petrology and geothermobarometry of granulite facies metapelites from the Hisøy-Torungen area, South Norway; new data on the Sveconorvegian P-T-t path of the Bamble sector. Journal of Metamorphic Geology, 14(3): 267-287.

Konnerup-Madsen, J., 1979. Fluid Inclusions in Quartz from Deep-Seated Granitic Intrusions, South-Norway. Lithos, 12(1): 13-23.

Krumgalz, B.S., Pogorelsky, R. and Pitzer, K.S., 1996. Volumetric properties of single aqueous electrolytes from zero to saturation concentration at 298.15 degrees K represented by Pitzer's ion-interaction equations. Journal of Physical and Chemical Reference Data, 25(2): 663-689.

Kullerud, K., 1995. Chlorine, titanium and barium-rich biotites - Factors controlling biotite composition and the Implications for garnet-biotite geothermometry. Contributions to Mineralogy and Petrology, 120(1): 42-59.

Munz, I.A., Wayne, D. and Austrheim, H., 1994. Retrograde fluid infiltration in the high-grade Modum Complex, South Norway - Evidence for age, source and REE mobility. Contributions to Mineralogy and Petrology, 116(1-2): 32-46.

Munz, I.A., Yardley, B.W.D., Banks, D.A. and Wayne, D., 1995. Deep penetration of sedimentary fluids in basement rocks from Southern Norway - Evidence from hydrocarbon and brine inclusions in quartz veins. Geochimica Et Cosmochimica Acta, 59(2): 239-254.

Munz, I.A., Yardley, B.W.D. and Gleeson, S.A., 2002. Petroleum infiltration of high-grade basement, South Norway: Pressure-temperature-time-composition (P-T-t-X) constraints. Geofluids, 2(1): 41-53.

Newton, R.C., Charlu, T.V. and Kleppa, O.J., 1980. Thermochemistry of the high structural state plagioclases. Geochimica Et Cosmochimica Acta, 44(7): 933-941.

Newton, R.C. and Manning, C.E., 2000. Quartz solubility in H_2O-NaCl and H_2O-CO_2 solutions at deep crust-upper mantle pressures and temperatures: 2-15 kbar and 500-900 degrees C. Geochimica Et Cosmochimica Acta, 64(17): 2993-3005.

Nijland, T.G., Liauw, F., Visser, D., Maijer, C. and Senior, A., 1993. Metamorphic petrology of the Froland corundum-bearing rocks; the cooling and uplift history of the Bamble sector, South Norway. Bulletin - Norges Geologiske Undersokelse, 424: 51-63.

Nijland, T.G. and Maijer, C., 1993. The regional amphibolite to granulite facies transition at Arendal, Norway; evidence for a thermal dome. Neues Jahrbuch fuer Mineralogie Abhandlungen, 165: 191-221.

Nijland, T.G. and Touret, J.L.R., 2001. Replacement of graphic pegmatite by graphic albite-actinolite-clinopyroxene intergrowths (Mjavatn, southern Norway). European Journal of Mineralogy, 13(1): 41-50.

Nijland, T.G., Touret, J.L.R. and Visser, D., 1998. Anomalously low temperature orthopyroxene, spinel, and sapphirine occurrences in metasediments from the Bamble amphibolite-to-granulite facies transition zone (South Norway); possible evidence for localized action of saline fluids. Journal of Geology, 106(5): 575-590.

Powell, R. and Holland, T., 1999. Relating formulations of the thermodynamics of mineral solid solutions: Activity modeling of pyroxenes, amphiboles, and micas. American Mineralogist, 84(1-2): 1-14.

Rosing, M.T., Bird, D.K. and Dymek, R.F., 1987. Hydration of Corundum-Bearing Xenoliths in the Qorqut Granite Complex, Godthabsfjord, West Greenland. American Mineralogist, 72(1-2): 29-38.

Shmulovich, K.I., Yardley, B.W.D. and Graham, C.M., 2006. Solubility of quartz in crustal fluids: experiments and general equations for salt solutions and H2O-CO2 mixtures at 400-800 degrees C and 0.1-0.9 GPa. Geofluids, 6(2): 154-167.

Sørensen, B.E. and Larsen, R.B., 2007. Paper1: Fluid induced multistage recrystallisation microstructures in quartzites and quartz veins from the Bamble shear zone complex. In: B.E. Sørensen (Editor), Metamorphic refinement of quartz under influence of fluids during exhumation with reference to the metamorphic/metasomatic evolution observed in amphibolites - a detailed field, microtectonic and geochemical study

from the Bamble sector, South Norway. PhD Thesis, Department of Geology and Mineral Resources Engineering, NTNU Trondheim.

Sørensen, B.E., Larsen, R.B. and Austrheim, H., 2007. Paper3: Metasomatic evolution of the Froland amphibolites during cooling and uplift - textural observations and geochemical evolution of hydrous minerals. In: B.E. Sørensen (Editor), Metamorphic refinement of quartz under influence of fluids during exhumation with reference to the metamorphic/metasomatic evolution observed in amphibolites - a detailed field, microtectonic and geochemical study from the Bamble sector, South Norway. PhD Thesis, Department of Geology and Mineral Resources Engineering, NTNU Trondheim.

Stuwe, K., 1997. Effective bulk composition changes due to cooling: a model predicting complexities in retrograde reaction textures. Contributions to Mineralogy and Petrology, 129(1): 43-52.

Touret, J., 1968. The Precambrian metamorphic rocks around the Lake Vegår (Aust-Agder, southern Norway). Norges Geologiske Undersøkelse, 257, 45 pp.

Touret, J., 1971. Le faciès granulite en Norvège méridionale II Les inclusions fluides. Lithos, 4: 423-436.

Touret, J., 1985. Fluid regime in southern Norway: the record of fluid inclusions. In: A.C. Tobi and J. Touret (Editors), The deep Proterozoic crust in the North Atlantic Provinces NATO ASI Ser. Ser. C: Math. Phys. Sci., pp. 517-549.

Touret, J. and Olsen, S.N., 1985. Fluid inclusions in migmatites. In: J.R. Ashworth (Editor), Migmatites. Shiva, Glasgow, pp. 265-288.

Van den Kerkhof, A. and Thiery, R., 2001. Carbonic inclusions. Lithos, 55(1-4): 49-68.

Vanko, D.A., Bodnar, R.J. and Sterner, S.M., 1988. Synthetic fluid inclusions: VIII. Vapor-saturated halite solubility in part of the system NaCl-CaCl2-H2O, with application to fluid inclusions from oceanic hydrothermal systems. Geochimica et Cosmochimica Acta, 52(10): 2451-2456.

Wark, D. and Watson, E.B., 2006. TitaniQ: a titanium-in-quartz geothermometer Contributions to Mineralogy and Petrology, 152(6): 743-754.

Watson, E.B. and Brenan, J.M., 1987. Fluids in the Lithosphere, 1. Experimentally determined wetting characteristics of CO_2-H_2O fluids and their implications for fluid transport, host-rock physical properties,

and fluid inclusion formation. Earth Planet Scientific Letters, 85: 496-515.

Williams, J.A.E. and Samson, I.M., 1990. Theoretical estimation of halite solubility in the system NaCl-$CaCl_2$-H_2O; applications to fluid inclusions. The Canadian Mineralogist, 28(2): 299-304.

Zhang, Y.G. and Frantz, J.D., 1987. Determination of the Homogenization Temperatures and Densities of Supercritical Fluids in the System NaCl-KCl-$CaCl_2$-H_2O Using Synthetic Fluid Inclusions. Chemical Geology, 64(3-4): 335-350.